

Ferric iron in magmatic clinopyroxene, Part II: iron valence systematics in clinopyroxene crystals from ocean island basalts with implications for oxybarometry

David A. Neave*, Alexander G. Stewart, Margaret E. Hartley, Olivier Namur

*david.neave@manchester.ac.uk

This is a non-peer reviewed preprint of an article submitted for publication in Contributions to Mineralogy and Petrology and uploaded to EarthArXiv in June 2023.

Ferric iron in magmatic clinopyroxene, Part II: iron valence systematics in clinopyroxene crystals from ocean island basalts with implications for oxybarometry

David A. Neave^{1*}, Alexander G. Stewart¹, Margaret E. Hartley¹,
Olivier Namur²

^{1*}Department of Earth and Environmental Sciences, The University of
Manchester, Manchester, M13 9PL, United Kingdom.

²Department of Earth and Environmental Sciences, KU Leuven,
BE-3001 Leuven, Belgium.

*Corresponding author(s). E-mail(s): david.neave@manchester.ac.uk;

Abstract

Iron plays a vital role in both setting and recording the oxidation stage of magmatic systems, which is commonly expressed in terms of oxygen fugacity (f_{O_2}). Magmatic f_{O_2} varies between different tectonic settings and controls the trajectories along which magmas evolve and the properties of the volcanic gases they release into the atmosphere. Ocean island basalts (OIBs) derived at least in part from recycled mantle sources are increasingly thought to evolve under more oxidising conditions than mid-ocean ridge basalts (MORBs) from relatively depleted sources. However, the oxybarometric tools currently at our disposal are subject to a range of limitations, meaning that there are relatively few internally consistent estimates of f_{O_2} across multiple settings. Our understanding of the nature and causes of f_{O_2} variability within and between magmatic systems therefore remains limited. In Part I we demonstrated that previously discredited approaches for estimating clinopyroxene ferric iron contents can return comparably precise results to Mössbauer spectroscopy by optimising electron probe microanalysis techniques, raising the prospect of developing clinopyroxene-based oxybarometers. Here we present high-quality analyses of clinopyroxene crystals from OIBs erupted in Iceland and the Azores to determine their iron valence systematics and explore their potential use for oxybarometry. Although many studies assume that all iron in magmatic clinopyroxene crystals occurs as ferrous iron, we find that up to 50% of the total iron in magmatic clinopyroxene

crystals may be ferric iron, with crystals from alkali systems typically containing more ferric iron than those from tholeiitic systems. Most ferric iron is hosted within esseneite component ($\text{CaFe}^{3+}\text{AlSiO}_6$), though some may also be hosted in aegirine component ($\text{NaFe}^{3+}\text{Si}_2\text{O}_6$) in the most alkali crystals. Iron–magnesium exchange equilibria between clinopyroxene crystals and their host glasses return plausible f_{O_2} estimates for a tholeiitic basalt from Holuhraun in Iceland and an alkali basalt from Pico in the Azores but are subject to considerable uncertainties because the influence of ferric iron on clinopyroxene–liquid equilibria are poorly understood. There is no current advantage in accounting for ferric iron when evaluating iron–magnesium exchange between clinopyroxene–glass pairs. Magmatic f_{O_2} was also estimated by applying a recent parametrisation of ferric iron partitioning to determine the valence of iron in liquids in equilibrium with clinopyroxene crystals from Holuhraun and Pico. We infer that our samples from Holuhraun and Pico evolved at about one and half and two and a half log units above FMQ equilibrium, respectively. These values are in line with independent estimates from these eruptions and similar eruptions of OIB elsewhere, and demonstrate the considerable potential for further development of clinopyroxene-based oxybarometers.

Keywords: clinopyroxene, ferric iron, ocean island basalt, oxygen fugacity

1 Introduction

Iron is the most abundant multivalent element in terrestrial magmas and thus plays a central role in setting and recording magmatic oxygen fugacity (f_{O_2}) conditions (Frost, 1991), where f_{O_2} reflects the chemical potential of oxygen in a magma and therefore its redox state. For example, the f_{O_2} of naturally observed basaltic liquids extends from approximately one log unit below to two units above the fayalite–magnetite–quartz equilibrium (i.e., from FMQ–1 to FMQ+2) as the ratio of ferric to total Fe ($\text{Fe}^{3+}/\Sigma\text{Fe}$, where $\Sigma\text{Fe} = \text{Fe}^{2+} + \text{Fe}^{3+}$) increases from ~ 0.1 to ~ 0.3 (e.g., Cottrell et al, 2022), though the exact nature of this relationship is somewhat model dependant (Kress and Carmichael, 1991; O’Neill et al, 2018; Borisov et al, 2018). Understanding such coupled variations in $\text{Fe}^{3+}/\Sigma\text{Fe}$ and f_{O_2} is important because they exert a first-order control over phase equilibria (e.g., Toplis and Carroll, 1995; Feig et al, 2010), volatile solubilities (e.g., Jugo, 2009; O’Neill, 2021; Hughes et al, 2023) and volcanic gas compositions (e.g., Burgisser and Scaillet, 2007; Oppenheimer et al, 2011). They also played a central role in controlling the partitioning of elements between Earth’s geochemical reservoirs during planetary accretion and core segregation that has shaped much of its subsequent evolution (e.g., Wood et al, 2006). Magmatic f_{O_2} thus determines the trajectories along which magmas evolve, the nature of the cumulates they produce, and the abundance and speciation of the volatiles they release, which in turn affect ore formation processes and the evolution of planetary habitability through geological time (Holland, 2002; Evans and Tomkins, 2011; Gaillard et al, 2011).

Magmas erupted in different tectonic settings often record evolution under different f_{O_2} conditions (Carmichael, 1991; Cottrell et al, 2022). It is generally accepted

that most arc basalts evolve under more oxidising conditions (\sim FMQ+1) than mid-ocean ridge basalts (MORBs; \sim FMQ), even if the reasons for this remain contested and uncertain (Kelley and Cottrell, 2009; Gaetani, 2016; Brounce et al, 2019; Cottrell et al, 2022). Many ocean island basalts (OIBs) also record evolution under more oxidising conditions than MORBs, though the MORB-OIB dichotomy is decidedly more ambiguous than the MORB-arc dichotomy. Observations from the Canary Islands (Lanzarote and El Hierro), Cape Verde (Fogo) and Erebus suggest that some OIBs evolve at FMQ+2 or higher depending on the oxybarometer used (Moussallam et al, 2014, 2019; Taracsák et al, 2022). Observations from Iceland (Laki) and Hawaii (Kīlauea and Mauna Kea) also imply evolution under elevated f_{O_2} conditions that extend up to FMQ+1 (Moussallam et al, 2016; Brounce et al, 2017). Moreover, basalts from the Reykjanes Ridge record a slight increase in f_{O_2} as they approach Iceland, suggesting that f_{O_2} and $Fe^{3+}/\Sigma Fe$ are at least partly controlled by proximity to a mantle plume in this setting (Shorttle et al, 2015). In contrast, OIBs from Réunion appear to have evolved under comparable f_{O_2} conditions to MORB at or slightly below FMQ equilibrium (Brounce et al, 2022). While this variability may appear challenging to reconcile, Brounce et al (2022) provide a straightforward explanation that draws on known geochemical differences between different ocean island systems. Specifically, they argue that relatively oxidised OIBs are seemingly derived from mantle sources rich in recycled components (EM1, EM2 and HIMU), while relatively reduced OIBs are derived from mantle sources poor in recycled components (C/FOZO/PREMA; Zindler and Hart, 1986; Stracke, 2012). Nevertheless, internally consistent estimates of magmatic f_{O_2} conditions across different ocean island systems remain relatively scarce. Generating internally consistent datasets from diverse OIBs and MORBs is a key step towards understanding the significance of apparent f_{O_2} variability between different OIBs. We aim to start this process by investigating OIBs from Iceland and the Azores as a foundation for subsequent work in additional settings.

Considerable progress has been made in using mineral and glass compositions to estimate magmatic f_{O_2} conditions over recent decades, with two-oxide oxybarometry and Fe-XANES spectroscopy of volcanic glasses being especially fruitful (Cottrell et al, 2022, and references therein). However, the former depends on the presence of equilibrium magnetite and ilmenite pairs (e.g., Bacon and Druitt, 1988; Ghiorso and Evans, 2008), and the latter relies on the presence of pristine volcanic glass (e.g., Cottrell et al, 2009). Furthermore, Fe-XANES spectroscopy on glasses is complicated by possible electron exchanges between Fe and S on quenching (Nash et al, 2019) and the reduction of magmatic liquids by S degassing during magma ascent (Moussallam et al, 2016; Brounce et al, 2017). The sensitivity of hydrous glasses to beam damage adds further complexity (Cottrell et al, 2018). Moreover, Fe-XANES spectroscopy requires access to a synchrotron radiation source which can be challenging to secure. Fortunately, different f_{O_2} -sensitive mineral-mineral or mineral-liquid equilibria can allow us to circumvent these issues and recover better estimates of magmatic f_{O_2} , especially if the time taken for minerals to respond to syn- or post-eruptive changes in f_{O_2} is slow. Recent re-evaluations of olivine-liquid equilibria that have explicitly addressed challenges in parametrising Fe^{2+} -Mg exchange (i.e., $K_{D,Fe^{2+}-Mg}^{ol-liq}$) in systems with

variable glass $\text{Fe}^{3+}/\Sigma\text{Fe}$ contents provide one potential avenue for robust oxybarometry (Blundy et al, 2020; Saper et al, 2022). Here we aim to explore the feasibility of developing similar tools based on clinopyroxene–liquid equilibria.

Magmatic clinopyroxene crystals incorporate both Fe^{2+} and Fe^{3+} by virtue of their diverse cation sites: clinopyroxene has the general formula $\text{M2}(\text{R}^{2+})\text{M1}(\text{R}^{2+})\text{T}_2(2\text{R}^{4+})\text{O}_6$, where R is a metal cation, M2 is a distorted octahedral site, M1 is a regular octahedral site and T is a tetrahedral site typically occupied by Si forming the Si_2O_6 chains that define the pyroxene structure (Morimoto et al, 1988). As a consequence, clinopyroxene is inherently sensitive to the f_{O_2} conditions prevailing during its formation and should thus be well suited for use in oxybarometric tools. Moreover, clinopyroxene is a major constituent of diverse upper mantle and crustal rocks across all tectonic settings meaning. Clinopyroxene-based oxybarometers would thus be of widespread use, much like the increasingly large family of clinopyroxene-based barometers used for estimating magma storage pressures (e.g., Putirka et al, 1996; Putirka, 2008; Neave and Putirka, 2017; Wang et al, 2021). However, relatively little is known about iron valence systematics in natural clinopyroxene crystals, which fundamentally limits our ability to develop clinopyroxene oxybarometers. This primarily reflects the challenges associated with determining iron valence in clinopyroxene directly, whether by bulk methods or *in-situ* microanalysis requiring access to Mössbauer spectroscopy or a synchrotron radiation source (Canil and O’Neill, 1996; McCanta et al, 2004; Rudra et al, 2021; Rudra and Hirschmann, 2022; McCammon, 2021).

In Part I we critically re-evaluated previously discredited approaches for estimating clinopyroxene Fe^{3+} contents using stoichiometric constraints (cf., McGuire et al, 1989; Canil and O’Neill, 1996). By optimising the electron probe microanalysis (EPMA) technique used to measure clinopyroxene crystals (described in Part I and below), we demonstrated that clinopyroxene $\text{Fe}^{3+}/\Sigma\text{Fe}$ contents determined using the stoichiometric approach of Droop (1987) have a similar precision to those derived from Mössbauer spectroscopy. Using with these robust estimates of clinopyroxene $\text{Fe}^{3+}/\Sigma\text{Fe}$ contents we then showed that more than half of the Fe present in natural augite crystals (with a nominal formula of $\text{Ca}(\text{Mg},\text{Fe}^{2+})\text{Si}_2\text{O}_6$) can occur as Fe^{3+} , in line with sparse analyses of augite crystals in mafic alkaline rocks by Mössbauer spectroscopy (McGuire et al, 1989; Weis et al, 2015). We therefore devised a new scheme for assigning clinopyroxene components that explicitly accounts for the presence of Fe^{3+} . Specifically we advocated assigning most Fe^{3+} to an esseneite component (Es, $\text{CaFe}^{3+}\text{AlSiO}_6$) via a Tschermak-type substitution, with some Fe^{3+} potentially being assigned to an aegirine component (Ae, $\text{NaFe}^{3+}\text{Si}_2\text{O}_6$) formed from excess Na after forming jadeite component (Jd, $\text{NaAlSi}_2\text{O}_6$), especially in alkali-rich crystals. One key aim of the present study is to use this new scheme to provide the first systematic survey of clinopyroxene components in crystals from diverse OIBs that specifically addresses the presence of Fe^{3+} . Only by developing this better understanding of clinopyroxene Fe^{3+} systematics is it possible to meaningfully investigate how clinopyroxene reflects magmatic f_{O_2} .

Here we present high-precision EPMA analyses of clinopyroxene crystals in OIBs from Iceland and the Azores from which clinopyroxene $\text{Fe}^{3+}/\Sigma\text{Fe}$ contents have been

estimated using the stoichiometric approaches validated in Part I. By applying our revised scheme for assigning clinopyroxene components to these basalts, we show how Fe^{3+} is an important constituent of clinopyroxene crystals from diverse natural magmas. Finally, we use our improved understanding of clinopyroxene $\text{Fe}^{3+}/\Sigma\text{Fe}$ in magmatic systems to explore the considerable potential for clinopyroxene oxybarometry within the scope of currently available partitioning models. While subject to numerous limitations, our findings suggest that clinopyroxene Fe^{3+} can successfully record oxybarometric information, with OIBs from Iceland and the Azores evolving under more oxidising conditions than expected for MORB.

2 Samples

We studied six OIBs erupted from well-characterised but geochemically distinct magmatic systems in the North Atlantic (Figure 1). We investigated samples ranging from tholeiitic to alkali basalts and ankaramites in order to evaluate major element controls on clinopyroxene compositions and the effects of anticipated variations in magmatic f_{O_2} conditions on clinopyroxene $\text{Fe}^{3+}/\Sigma\text{Fe}$ contents (Moussallam et al, 2019; Cottrell et al, 2022). Lava samples were cut into polished thin sections and tephra samples were mounted in epoxy prior to imaging and microanalysis.

Tholeiitic and moderately primitive (~ 7 wt.% MgO) pillow basalt samples (HOR-11-01 and SKU-11-18) were collected from Skuggafjöll mountain in the Eastern Volcanic Zone (EVZ) of southern Iceland. The petrology and geochemistry of these samples and Skuggafjöll as a whole are described by Neave et al (2014). Tholeiitic and moderately primitive (~ 7 wt.% MgO) basaltic tephra samples were collected from 2014–2015 Holuhraun eruption in the Northern Volcanic Zone (NVZ) of central Iceland. Our sample is equivalent to sample H14 described by Halldórsson et al (2018), who also described the petrology and geochemistry of the eruption as a whole. A tholeiitic and moderately evolved (~ 4.5 wt.% MgO) basaltic lava sample (LAK-04) was collected from the Laki lava flow in the EVZ southern Iceland. The petrology and geochemistry of LAK-04 and the wider Laki lava flow are described by Passmore et al (2012) and Neave et al (2013). Three ankaramite (highly olivine- and clinopyroxene-phyric alkali basalts) lava samples (HVAM13-01, ARN13-01 and HLTS13-01, from Hvammsmúli, Arnarholl and Holtsdalur, respectively) were collected from Eyjafjalljökull in the the EVZ of southern Iceland. The petrology of some of these ankaramite localities is described by Loughlin (1995) and Nikkola et al (2019).

An alkali basalt lava sample (PI-011) was collected from the northern flank of Pico volcano on Pico Island in the Azores. A trachybasaltic to tephritic tephra sample (PI-041) was also collected from a vent on the Panalto da Achada fissure system extending southeastwards from the central volcano. The petrology and geochemistry of Pico island are discussed in detail by França et al (2006) and Zanon et al (2020).

3 Methods

In preparation for electron probe microanalysis (EPMA), backscattered electron (BSE) images were collected from epoxy mounts and thin sections using a FEI Quanta 650F scanning electron microscope (SEM) in the Department of Earth and Environmental

Sciences at The University of Manchester. This imaging was undertaken to characterise compositional variability across our samples, and especially within clinopyroxene crystals that are often characterised by complex concentric and sector zoning.

Quantitative analyses of clinopyroxene, olivine, plagioclase, oxides and glass were performed by EPMA using a JEOL JXA8530F instrument in the School of Earth Sciences at the University of Bristol operated with Probe for EPMA (<https://www.probesoftware.com/>). The following primary standards were used for calibration: Si, albite; Ti, TiO₂; Al, sanidine; Cr, Cr₂O₃; Fe, hematite; Mn, Mn metal; Mg, St. John's olivine; Ca, wollastonite; Na, albite; K, sanidine; P, Durango apatite; and Ni, Ni metal.

Different analytical conditions were used for analysing different phases, with particular care taken over the analysis of clinopyroxene to ensure that Fe³⁺/ΣFe could be estimated reliably by stoichiometry. We used an accelerating voltage of 15 kV and a spot size of 1 μm to analyse clinopyroxene, olivine and oxides. The following elements were analysed with a current of 10 nA (on-peak counting times in seconds are shown in parentheses; background counting times were half on-peak counting times): Si(20), Ti(20), Al(20), Fe(40), Mg(40), Ca(20) and K(40); and the following elements were analysed with a current of 40 nA: Cr(60), Mn(30), Na(60), P(60) and Ni(30). We used this approach to maximise the precision of minor element analyses in clinopyroxene that affect the precision of thermobarometric calculations (Wieser et al, 2023), and likely affect the quality of clinopyroxene Fe³⁺/ΣFe contents estimated from stoichiometric constraints (Part I). Importantly, monitoring the time-dependent intensity of Na counts demonstrates that Na remains immobile when analysing clinopyroxene with a focused beam at 40 nA or even 100 nA (Wieser et al, 2023). All elements in plagioclase and glass were analysed with an accelerating voltage of 15 kV, a defocused 10 μm spot and a current of 10 nA (on-peak counting times in seconds are shown in parentheses; background counting times were half on-peak counting times): Si(10), Ti(50), Al(10), Cr(10), Fe(30), Mn(30), Mg(50), Ca(10), Na(10), K(10) and P(40).

Accuracy was monitored by analysing the following secondary standards: in-house diopside, Cr-diopside and labradorite, and international kk1 kaersutite (Reay et al, 1989), BCR-2G basaltic glass (Jochum et al, 2005). Major element (e.g., SiO₂ and MgO in glass and clinopyroxene) concentrations were typically within 2% of preferred values (based on published values or longitudinal data for in-house standards), while minor element (e.g., Cr₂O₃ and Na₂O in Cr-diopside and FeO_T in plagioclase) concentrations were typically within 6% of preferred values. Counting statistics from analyses of unknown clinopyroxene crystals indicate that major (SiO₂, Al₂O₃, FeO_T, MgO and CaO) and minor (TiO₂, Cr₂O₃ and Na₂O) elements were measured with 1σ precisions better than 1% and 5%, respectively; only MnO was measured with a worse 1σ precision of ~8%. Olivine, plagioclase, oxides and glass were measured with comparable 1σ precisions: better than 2% for major elements and better than 5% for most minor elements. Full details of secondary standard analyses and analytical precision are provided alongside all EPMA data in the Supplementary Material.

4 Results

4.1 Petrography

Tholeiitic pillow basalts HOR-11-01 and SKU-11-18 from Skuggafjöll contain macrocrysts of plagioclase, clinopyroxene and olivine in a glassy to microcrystalline and somewhat vesicular groundmass (Neave et al, 2014). Macrocrysts are defined as being $>100\ \mu\text{m}$ in length and texturally distinct from the groundmass (e.g., Thomson and MacLennan, 2013). Clinopyroxene macrocrysts are up to $\sim 500\ \mu\text{m}$ in length and often occur in ophitic arrangement with plagioclase. They typically show weak oscillatory zoning but prominent hourglass sector zoning with low-BSE-intensity $\{\bar{1}11\}$ sectors and high-BSE-intensity $\{hk0\}$ sectors (Figure 2A; Neave et al, 2019a).

The tholeiitic basalt tephra from Holuhraun contains macrocrysts of plagioclase, clinopyroxene and olivine in a glassy and highly vesicular groundmass (Halldórsson et al, 2018). Clinopyroxene macrocrysts are up to $\sim 250\ \mu\text{m}$ in length and often occur in ophitic arrangement with plagioclase, and also sometimes in association with olivine. Most show weak oscillatory and sector zoning, but the crystals are too small to show sector geometries at the resolution of BSE imaging (Figure 2B).

The tholeiitic basalt lava sample LAK04 from Laki contains macrocrysts of plagioclase, clinopyroxene and olivine in a microcrystalline and vesicular groundmass (Passmore et al, 2012; Neave et al, 2013). Clinopyroxene macrocrysts up to $\sim 800\ \mu\text{m}$ occur in ophitic arrangement with plagioclase, most often in multiphase glomerocrysts that also contain olivine and plagioclase macrocrysts (Figure 2C). Most crystals also show concentric and hourglass sector zoning like that observed for Skuggafjöll.

The ankaramitic lava samples HVAM13-01, ARN13-01 and HLTS13-01 from Eyjafjallajökull are dominated by large macrocrysts of olivine and clinopyroxene and smaller oxide macrocrysts in microcrystalline groundmasses, though some plagioclase macrocrysts occur in ARN13-01. Clinopyroxene macrocrysts up to $\sim 5\ \text{mm}$ in length typically occur as individual, euhedral to subhedral crystals, with some occurring in association with olivine (Figure 2D). Most clinopyroxene crystals are characterised by simple core-rim zoning, though crystals in HVAM13-01 appear to show reaction rims consistent with dissolution prior to final solidification (e.g., Neave and MacLennan, 2020).

The alkali basalt lava PI-011 from Pico contains large macrocrysts of clinopyroxene, olivine, plagioclase, magnetite and ilmenite in a microcrystalline and vesicular groundmass that also contains microcrysts (crystals $<100\ \mu\text{m}$ in length that are distinct from the groundmass) of the same phases. Clinopyroxene macrocrysts up to $\sim 4\ \text{mm}$ in length generally occur as individual, euhedral crystals, though some occur in glomerocrysts with olivine and/or plagioclase. Most crystals show slight core-to-rim zoning overlain onto complex and patchy sector zoning (Figure 2E).

The alkali basalt tephra sample PI-041 from Pico contains macrocrysts of clinopyroxene, olivine, plagioclase, magnetite and ilmenite in a glassy and highly vesicular groundmass that also contains microcrysts of the same phases. Clinopyroxene macrocrysts up to $\sim 2\ \text{mm}$ in length generally occur as individual, euhedral to subhedral crystals, though some occur in association with olivine and ilmenite. Clinopyroxene crystals show optical evidence for both core-to-rim zoning and complex, patchy sector zoning (Figure 2F).

4.2 Major element chemistry

The major element chemistry of clinopyroxene crystals in our OIB samples is summarised in a series of pyroxene quadrilaterals in Figure 3; all crystals plot firmly in the quadrilateral field of a Q–J diagram (Morimoto et al, 1988). In Figure 3A we follow the established convention of Morimoto et al (1988) in calculating the Fe component (ΣFe^*) as the sum of Fe^{2+} , Fe^{3+} and Mn. However, Fe^{3+} is not incorporated into the quadrilateral components (diopside, Di, $\text{CaMgSi}_2\text{O}_6$; hedenbergite, Hd, $\text{CaFe}^{2+}\text{Si}_2\text{O}_6$; enstatite, En, MgSiO_3 or ferrosilite, Fs, $\text{Fe}^{2+}\text{SiO}_3$); quadrilateral components only incorporate divalent cations on their M2 and M1 sites. In Figure 3B we therefore show pyroxene quadrilaterals plotted with a modified Fe component (ΣFe^\dagger) calculated from the sum of Fe^{2+} estimated following Droop (1987) and Mn. Clinopyroxene crystals from each of our OIB samples define distinct populations in both Figures 3A and 3B.

Clinopyroxene crystals in tholeiitic samples from Laki, Holuhraun and Skuggafjöll define an approximate differentiation trend (Figure 3), with those from Skuggafjöll being the most primitive (highest Di content and therefore highest Mg#, where $\text{Mg\#} = \text{Mg}/(\text{Mg} + \text{Fe}^{2+})$ on a molar basis, with Fe^{2+} estimated following Droop (1987)), those from Holuhraun being slightly more evolved, and those from Laki being the most evolved (lowest Di and Mg#). Although Di and Hd dominate, all clinopyroxene crystals from tholeiitic basalts contain some En and Fs that increase in abundance with increasing degrees of evolution (i.e., decreasing Mg#). Clinopyroxene crystals from Skuggafjöll show the greatest variability in DiHd versus EnFs contents, consistent with the presence of significant sector zoning (Neave et al, 2019a). Clinopyroxene crystals from Laki show the greatest overall spread in compositions, consistent with the protracted magmatic history recorded by these crystals (Neave et al, 2013). Removing Fe^{3+} from the calculation of quadrilateral components has no significant effect beyond moving all data slightly towards the Di apex.

Despite erupting from two geographically distinct systems, clinopyroxene crystals in alkali samples from Pico and Eyjafjallajökull also form an approximate differentiation trend (Figure 3). However, although the most primitive clinopyroxene crystals from Eyjafjallajökull and Pico (PI-011 in particular) lie close to some crystals from the tholeiitic Skuggafjöll eruption in quadrilateral space, more evolved clinopyroxene crystals from Eyjafjallajökull and Pico (PI-041 in particular) lie much closer to the Di–Hd tie line than relatively evolved clinopyroxene crystals from the tholeiitic Holuhraun and Laki eruptions. That is, clinopyroxene crystals from alkali samples seem to evolve towards higher DiHd, while those from tholeiitic samples evolve to lower DiHd contents. This effect is especially pronounced when Fe^{3+} is removed from the calculation of quadrilateral components and clinopyroxene compositions move towards the Di apex. Some clinopyroxene crystals from PI-041 then land above the Di–Hd tie line, likely because of the greater contribution of Ca to non-quadrilateral components in clinopyroxene crystals from alkali samples with respect to those from tholeiitic samples (e.g., Robinson, 1980).

Clinopyroxene crystals from alkali samples contain higher Na_2O contents than those from the tholeiitic samples ($\sim 0.3\text{--}0.6$ wt.% versus $\sim 0.15\text{--}0.3$ wt.%; Figure 4A). Overall there is a strong correlation between MgO and Na_2O , though clinopyroxene crystals from different eruptions define slightly offset arrays. Although significant (>1

wt.%) concentrations of Cr_2O_3 are only found in relatively primitive clinopyroxene crystals (Figure 4B), analyses from both alkali and tholeiitic samples define the same broad trend; evolved clinopyroxene crystals contain negligible Cr_2O_3 . Clinopyroxene crystals from different eruptions are characterised by different but often remarkably constant Ti:Al values. Overall, clinopyroxene crystals from alkali samples have higher Ti:Al than those from tholeiitic samples, with the exception of clinopyroxene crystals from the evolved and tholeiitic Laki eruption that overlap with clinopyroxene crystals in alkali ankaramites from Eyjafjallajökull.

4.3 Iron valence systematics

The concentration and valence systematics of Fe in clinopyroxene crystals from our OIB samples are summarised in Figure 5. Distinct crystal lines of descent identified on pyroxene quadrilaterals are reproduced on a plot of MgO versus total Fe expressed as FeO (FeO_T ; Figure 5A). Clinopyroxene crystals from tholeiitic eruptions at Skuggafjöll, Holuhraun and Laki define a relatively steep trend in increasing FeO_T with decreasing MgO (with the highest FeO_T contents found in clinopyroxene rims from Laki), while clinopyroxene crystals from alkali eruptions on Pico define a shallower trend; clinopyroxene crystals from Eyjafjallajökull fall between these two trends. However, trends are weaker when MgO is plotted against FeO determined by stoichiometry following Droop (1987) (Figure 5B). For example, clinopyroxene crystals from Skuggafjöll and Laki contain ~ 1 and ~ 2 wt.% less FeO than FeO_T , respectively, while FeO and FeO_T are broadly comparable in clinopyroxene crystals from Holuhraun. Conversely, the enrichment in FeO with decreasing MgO is markedly less coherent than the enrichment in FeO_T .

Clinopyroxene Fe_2O_3 contents determined following Droop (1987) are summarised as a function of MgO in Figure 5C. Clinopyroxene Fe_2O_3 contents vary from within uncertainty of 0 wt.% (where 1σ uncertainties of ~ 0.35 wt.% were obtained using a Monte-Carlo approach described in Part I) to ~ 4.5 wt.%, meaning that Fe_2O_3 is a significant constituent of many clinopyroxene crystals from OIBs. Alongside Al, Fe^{3+} is, therefore, probably the most abundant cation in magmatic clinopyroxene crystals after those that form quadrilateral components (Si, Ca, Mg and Fe^{2+}). Overall, Fe_2O_3 contents are generally much lower in primitive clinopyroxene crystals with higher MgO contents (~ 1 wt.% at 17 wt.% MgO) than evolved clinopyroxene crystals with lower MgO contents (~ 4 wt.% at 13 wt.% MgO). To first order, clinopyroxene crystals from tholeiitic and alkali systems lie on the same trend. In detail, however, more structure arises. For example, clinopyroxene crystals from Holuhraun contain the lowest Fe_2O_3 contents, which rarely exceed 1 wt.% and are often within uncertainty of 0 wt.%; clinopyroxene crystals from Skuggafjöll contain ~ 1 wt.% more Fe_2O_3 than those from Holuhraun. Many clinopyroxene crystals from alkali samples are relatively evolved and contain high Fe_2O_3 contents that overlap with values from Skuggafjöll and Laki (1–2 wt.%) at their lower limit of but extend to much higher values (~ 4.5 wt.%) at their upper limit. On average, clinopyroxene crystals from Eyjafjallajökull reach any given Fe_2O_3 at a higher MgO content than those from Pico. Rim and microcryst compositions from sample PI-041 extend from the main trend to low Fe_2O_3 (within uncertainty of 0 wt.%) at a constant MgO (~ 13 wt.%).

Clinopyroxene $\text{Fe}^{3+}/\Sigma\text{Fe}$ contents estimated following the stoichiometric approach of Droop (1987) are summarised as a function of MgO in Figure 5D. These $\text{Fe}^{3+}/\Sigma\text{Fe}$ contents are typically subject to 1σ uncertainties on the order of 0.03 according to a Monte-Carlo approach described in Part I. Importantly, we estimate that these 1σ uncertainties would have been at least a factor of three larger if EPMA had been performed under more routine conditions whereby minor elements were counted for 10 s at 10 nA (e.g., Neave et al, 2019a). Overall, clinopyroxene $\text{Fe}^{3+}/\Sigma\text{Fe}$ contents extend from ~ 0 –0.3 in primitive crystals from Skuggafjöll and Holuhraun, with the latter having lower values mostly limited to 0–0.1, to ~ 0.4 and ~ 0.5 in evolved crystals from Eyjafjallajökull and Pico, respectively. Importantly, these high values are consistent with high-precision analyses on clinopyroxene crystals in mafic alkali rocks from the Canary Islands by Mössbauer spectroscopy that yield $\text{Fe}^{3+}/\Sigma\text{Fe}$ contents of 0.49–0.63 (Weis et al, 2015). Variations in $\text{Fe}^{3+}/\Sigma\text{Fe}$ are nonetheless considerable at any given MgO for any given eruption (≥ 0.3). However, in contrast with McGuire et al (1989) who ascribed similarly variable clinopyroxene $\text{Fe}^{3+}/\Sigma\text{Fe}$ contents to fundamental limits with the technique, we believe that much of this variability is geological in origin. Our reasons for this are threefold: firstly, the close correspondence between $\text{Fe}^{3+}/\Sigma\text{Fe}$ contents determined by Mössbauer and stoichiometry in endmember and single-crystal clinopyroxenes suggests that the latter are reliable (Part I); secondly, Monte Carlo-derived estimates of uncertainties in $\text{Fe}^{3+}/\Sigma\text{Fe}$ are smaller than the variability observed (1σ uncertainties of ~ 0.03 are an order of magnitude smaller than natural variability of ≥ 0.3 at any given MgO); and finally, our knowledge of clinopyroxene chemistry has grown considerably in recent decades. In particular, we now have a much greater understanding of how kinetics and sector zone development generate compositional variability independent of magmatic evolution and magma storage conditions, especially when considering the abundance and systematics of trivalent Al, which may serve as an analogue for Fe^{3+} (Mollo et al, 2010, 2018; Neave et al, 2019a; Ubide et al, 2019). Indeed, a central role for Al in mediating Fe^{3+} incorporation is implied in a recent parametrisation of Fe^{3+} partitioning between clinopyroxene and liquid, highlighting the potential importance of crystal chemical effects (Rudra and Hirschmann, 2022).

5 Discussion

5.1 Chemical systematics in clinopyroxene crystals from ocean island basalts

Clinopyroxene components calculated with the revised scheme described in Part I and summarised in the appendix are shown in Figure 6. These reveal considerable variability within and between clinopyroxene crystals from different OIBs. Clinopyroxene crystals from tholeiitic samples contain similar amounts of Jd, while the Jd content in crystals from alkali samples is larger and more variable (Figure 6A). Although it is unsurprising that clinopyroxenes from alkali-rich system contain more Na-bearing Jd, differences in Jd contents also reflect differences in magma storage pressures. Both Jd-based clinopyroxene-liquid barometry and Jd-independent volatile saturation barometry indicate that the tholeiitic magmas erupted at Skuggafjöll, Holuhraun

and Laki were stored at lower pressures prior to eruption (~ 200 MPa km; Neave and Putirka, 2017; Bali et al, 2018) than the alkali magmas erupted from Pico (~ 200 – 500 MPa; Zanon et al, 2020). The broadly intermediate Jd content of clinopyroxene crystals from Eyjafjallajökull reflects their storage intermediate depths (~ 300 MPa; Nikkola et al, 2019). As anticipated, relatively few clinopyroxene crystals contain much Ae; Figure 6B), with any Ae present restricted to Al^{VI}-poor analyses from Na-rich or low-Mg# crystals. Otherwise there are no clear systematics in the Ae content of clinopyroxene crystals from OIBs. In contrast with the assumptions of Lindsley (1983), Fe³⁺ does not appear to be hosted by Ae in most magmatic clinopyroxene crystals, examples from evolved alkali systems notwithstanding (cf., Larsen, 1976).

In line with their high Fe³⁺ but low Ae contents, we infer that Es is a major constituent of clinopyroxene crystals in our OIB samples (Figure 6C). With the exception of Fe³⁺-poor crystals from Holuhraun ($X_{Es} \sim 0$ – 0.03), the Es content of clinopyroxene crystals from tholeiitic and alkali magmas largely overlap, with the latter extending to slightly higher values (~ 0 – 0.07 versus ~ 0 – 0.10). The tempering of high Es contents in the highest-Fe³⁺ clinopyroxene crystals from alkali samples reflects the formation of minor Ae in some cases (Figure 6B). Nonetheless, the revised scheme for clinopyroxene componentry described in Part I implies that Es is the most abundant non-quadrilateral component in OIB clinopyroxene crystals.

The abundance of calcium Tschermak’s component (CaTs, CaAlAlSiO₆) varies substantially between clinopyroxene crystals from different samples (Figure 6D). Clinopyroxene crystals from Skuggafjöll and the alkali samples span a wide range in CaTs (~ 0 – 0.05). This likely reflects the prevalence of sector zoning, both hourglass and patchy, in these samples. Indeed, such zoning is largely defined by the variable partitioning of quadrilateral and non-quadrilateral components between different sectors (Ubide et al, 2019). In contrast, crystals from Laki have low CaTs contents, likely because of their relatively high Jd contents, while those from Na-poor Holuhraun have high CaTs contents. Although high CaTs contents can reflect disequilibrium crystallisation in some clinopyroxenes, this does not appear to be the case in crystals from Holuhraun (Neave et al, 2019a).

The abundance of titanium pyroxene component (CaTi, CaTiAl₂O₆) varies significantly between different samples (Figure 6E). Clinopyroxene crystals from tholeiitic samples form an approximate differentiation trend at relatively low CaTi for any given Mg# (evolving from ~ 0.01 at Mg# = 0.9 to ~ 0.04 at Mg# = 0.75), while clinopyroxene crystals in alkali samples from Pico evolve towards much higher CaTi (from ~ 0.02 at Mg# = 0.9 to ~ 0.08 at Mg# = 0.75). Clinopyroxenes from Eyjafjallajökull define a somewhat intermediate trend that partly overlaps with that defined by crystals from Pico. These trends not only reflect the way in which Ti tracks magmatic evolution in clinopyroxene, but also the close association of Ti with Al in clinopyroxene crystals from alkali magmas (Leung, 1974; Ubide et al, 2019) that is generally conserved across different sector zones (e.g., Downes, 1974). The incorporation of Ti alongside 2Al^{IV} is consistent with Ti:Al ratios in excess of 1:2 (Figure 4C), leaving excess Al to form other components. We also note that calculating CaTi from Ti rather than residual Al^{IV} as suggested by Putirka et al (1996) is essential for recovering clinopyroxene Ti systematics accurately; calculating from Al^{IV} could result in overestimating

apparent CaTi contents. Finally, although there is no need to form other Ti-bearing components such as neptunite (Np , $\text{NaFe}_{0.5}^{2+}\text{Ti}_{0.5}\text{Si}_2\text{O}_6$), its Mg-bearing equivalent ($\text{NaMg}_{0.5}\text{Ti}_{0.5}\text{Si}_2\text{O}_6$) or the fictive aluminobuffonite (ABf , $\text{CaMg}_{0.5}\text{Ti}_{0.5}\text{AlSiO}_6$) of [Sack and Ghiorso \(1994\)](#) to account for the compositions of our clinopyroxene crystals, there is scope for additional coupled substitutions that are not captured by our componentry scheme. Addressing this complexity would however require a thermodynamic approach that is beyond the scope of this manuscript.

Significant amounts of chromian calcium-Tschermak’s component (CrAlTs , CaCrAlSiO_6) only occur in primitive, high-Mg# clinopyroxene crystals (Figure 6F), as expected for a component hosting a minor compatible element. Namely, CrAlTs contents rapidly decrease from ~ 0.03 to < 0.005 over a Mg# window of ~ 0.9 to 0.75 in clinopyroxene crystals from both tholeiitic and alkali samples. High CrAlTs contents are offset to higher Mg# in clinopyroxene crystals from Pico and Eyjafjallajökull than their tholeiitic equivalents because the high Fe^{3+} content of these crystals inflates calculated Mg# values.

As anticipated given their augitic compositions, all clinopyroxene crystals from our OIB samples are dominated by DiHd (Figure 6G). However, it is notable that the DiHd contents of clinopyroxene crystals from tholeiitic samples are generally lower than those from alkali samples ($0.64\text{--}0.76$ versus $0.70\text{--}0.80$, respectively). The DiHd content of clinopyroxene crystals from tholeiitic samples also decreases with decreasing Mg# in a manner consistent with the pyroxene solvus between DiHd and EnFs narrowing with decreasing temperature ([Lindsley and Andersen, 1983](#)). In contrast, the DiHd content of clinopyroxene crystals from alkali samples remains broadly constant with decreasing Mg#. Importantly, calculating DiHd in this manner accounts for the incorporation of Ca into non-quadrilateral components, meaning we do not observe the excess DiHd implied from pyroxene quadrilaterals plotted accounting for Fe^{3+} and shown in Figure 3B; the high and steady DiHd content with decreasing Mg# in clinopyroxene crystals from alkali samples is real. Unsurprisingly, the EnFs contents of our clinopyroxene crystals are almost perfectly antithetical to their DiHd contents, with the striking observation that X_{EnFs} does not increase at all with decreasing Mg# in clinopyroxene crystals from alkali samples.

5.2 Iron-magnesium exchange and clinopyroxene-liquid equilibria

Clinopyroxene crystals primarily record magmatic evolution as a transition from Mg-rich compositions that are dominated by Di to Fe-rich compositions that are dominated by Hd. As such, clinopyroxene-liquid equilibria are often summarised using Fe–Mg exchange equilibria expressed as $K_{\text{D,Fe-Mg}}^{\text{cpx-liq}}$ ([Wood and Blundy, 1997](#); [Putirka, 2008](#)). This convention arises at least partly because of similarities between clinopyroxene-liquid equilibria and more extensively studied olivine-liquid equilibria described using $K_{\text{D,Fe}^{2+}\text{-Mg}}^{\text{ol-liq}}$ values ([Roeder and Emslie, 1970](#); [Blundy et al, 2020](#); [Saper et al, 2022](#)). Equation 35 of [Putirka \(2008\)](#) provides the most recent description of $K_{\text{D,Fe-Mg}}^{\text{cpx-liq}}$ applicable to OIBs. Although this model incorporates the effect of temperature on $K_{\text{D,Fe-Mg}}^{\text{cpx-liq}}$, and returns a value of ~ 0.28 at temperatures relevant to OIB evolution

(1200 °C) that is close to values of ~ 0.27 from experiments on MORB compositions (Grove et al, 1992), it assumes that all Fe occurs as Fe^{2+} in both clinopyroxenes and liquids, hence our use of $K_{\text{D,Fe-Mg}}^{\text{cpx-liq}}$ rather than $K_{\text{D,Fe}^{2+}\text{-Mg}}^{\text{cpx-liq}}$. This assumption is clearly incorrect for basaltic liquids that are characterised by $\text{Fe}^{3+}/\Sigma\text{Fe}$ contents ranging from ~ 0.1 to ~ 0.3 across a naturally relevant range of f_{O_2} conditions (FMQ–1 to FMQ+2; Kress and Carmichael, 1991; Borisov et al, 2018). Our findings demonstrate that it is also incorrect from the crystal perspective, with clinopyroxene crystals from diverse OIBs exhibiting $\text{Fe}^{3+}/\Sigma\text{Fe}$ contents ranging from ~ 0 to ~ 0.5 (Figure 5D). Given that Fe^{2+} and Fe^{3+} are incorporated into clinopyroxene via different mechanisms, with Fe^{3+} unlikely to exchange with Mg, developing a rigorous understanding of clinopyroxene-liquid equilibria therefore requires a better knowledge of true $K_{\text{D,Fe}^{2+}\text{-Mg}}^{\text{cpx-liq}}$ systematics.

Two samples, Holuhraun and PI-041 from Pico, contain clinopyroxene crystals in textural equilibrium with their host glasses and are thus suitable for investigating Fe–Mg and Fe^{2+} –Mg exchanges in detail. We initially investigated samples from Skuggafjöll as well, but found evidence of clinopyroxene-liquid disequilibrium that eventually resulted in implausibly high f_{O_2} estimates for these samples (greater than FMQ+3) and therefore did not consider them further. Combined glass and clinopyroxene Mg# systematics are summarised for Holuhraun and PI-041 in Figure 7, onto which $K_{\text{D,Fe-Mg}}^{\text{cpx-liq}}$ contours have been overlain and the $K_{\text{D,Fe-Mg}}^{\text{cpx-liq}} = 0.28$ contour derived from Equation 35 of Putirka (2008) highlighted. Clinopyroxene analyses from Holuhraun were filtered to only include data from rims in $\{hk0\}$ sectors that formed under near-equilibrium conditions (Halldórsson et al, 2018; Neave et al, 2019a); $\{\bar{1}11\}$ sectors did not form under equilibrium conditions and were thus not considered suitable for investigating Fe–Mg or Fe^{2+} –Mg equilibria. Rim and microcryst analyses in feasible equilibrium with the matrix glass of PI-041 were identified texturally; compositionally distinct rims in contact with glasses are clear in clinopyroxene crystals from PI-041 (Figure 2F).

Clinopyroxene-liquid Fe–Mg equilibria calculated assuming that all Fe in both glasses and clinopyroxene crystals is Fe^{2+} are shown in all panels of Figure 7. Although clinopyroxene-glass pairs do not lie far from $K_{\text{D,Fe-Mg}}^{\text{cpx-liq}} = 0.28$, most lie to lower values. Equilibria calculated with glass $\text{Fe}^{3+}/\Sigma\text{Fe}$ contents adjusted to different f_{O_2} conditions according to the model of Borisov et al (2018) but clinopyroxene $\text{Fe}^{3+}/\Sigma\text{Fe}$ contents set to zero – as set of assumptions sometimes applied in petrological studies (e.g., Neave et al, 2019a) – are shown in Figures 7A, C and E. In these cases, clinopyroxene-glass pairs best approach $K_{\text{D,Fe-Mg}}^{\text{cpx-liq}} = 0.28$ at FMQ to FMQ+1 for Holuhraun and at FMQ+1 and FMQ+2 for PI-041 microcrysts and rims, respectively. Although such f_{O_2} conditions are plausible (Moussallam et al, 2019; Taracsák et al, 2022), they were not estimated on the basis of true Fe^{2+} –Mg exchange because we did not account for the presence of Fe^{3+} in clinopyroxene crystals.

True Fe^{2+} –Mg equilibria calculated with glass $\text{Fe}^{3+}/\Sigma\text{Fe}$ contents adjusted to different f_{O_2} conditions according to the model of Borisov et al (2018) and clinopyroxene $\text{Fe}^{3+}/\Sigma\text{Fe}$ contents estimated following Droop (1987) are shown in Figures 7B, D and F. Accounting for the presence Fe^{3+} shifts the Mg# of glasses and clinopyroxene crystals to higher values than when all Fe is assumed to occur as Fe^{2+} . This means that

apparent $K_{D,Fe-Mg}^{cpx-liq}$ values change less when Fe^{3+} is accounted for in both glasses and clinopyroxene crystals than when accounted for in glasses alone. Clinopyroxene-glass pairs straddle $K_{D,Fe-Mg}^{cpx-liq} = 0.28$ at FMQ+1 for Holuhraun, broadly consistent with estimates from S systematics (FMQ+0.5; [Bali et al, 2018](#)). Microcrysts and rims from PI-041 show different behaviours, with the former implying f_{O_2} conditions of FMQ+1 to FMQ+2, in line with published maxima from erupted OIB glasses ([Brounce et al, 2017](#); [Moussallam et al, 2019](#)), and the latter implying even higher f_{O_2} conditions of FMQ+3 or more, in line with vanadium partitioning oxybarometry performed on samples from El Hierro in the Canary Islands that were erupted in a similar tectonic setting ([Taracsák et al, 2022](#)). While the meaning of this dichotomy will be explored further in the following section, it highlights the important role of both liquid and clinopyroxene $Fe^{3+}/\Sigma Fe$ in controlling apparent $K_{D,Fe-Mg}^{cpx-liq}$ values. It also reveals our inadequate knowledge of Fe-Mg and Fe^{2+} -Mg clinopyroxene-liquid exchange equilibria more widely. Without further experiments to constrain the effect of variable clinopyroxene $Fe^{3+}/\Sigma Fe$ contents on $K_{D,Fe^{2+}-Mg}^{cpx-liq}$ specifically, it will remain unclear if Equation 35 of [Putirka \(2008\)](#) is reliable or not. Until then, and in contrast with our previous work ([Neave and Putirka, 2017](#); [Neave et al, 2019a](#)), we agree with [Wieser et al \(2022\)](#) that $K_{D,Fe-Mg}^{cpx-liq}$ should be evaluated with all Fe in both phases considered as Fe^{2+} .

5.3 Exploring the potential for clinopyroxene oxybarometry

The presence of significant Fe^{3+} in clinopyroxene crystals suggests that clinopyroxene may record widespread but current under-exploited archives of magmatic f_{O_2} . Indeed, the potential for clinopyroxene oxybarometry has been demonstrated for mantle samples investigated by Mössbauer spectroscopy ([Luth and Canil, 1993](#)). However, the previous section outlines how our understanding of $K_{D,Fe^{2+}-Mg}^{cpx-liq}$ is currently insufficient to perform oxybarometry analogous to the olivine-based approach described by [Blundy et al \(2020\)](#). Instead, we now explore the feasibility of exploiting clinopyroxene-liquid Fe^{3+} partitioning to estimate glass $Fe^{3+}/\Sigma Fe$ contents and thence f_{O_2} conditions.

The Al_2O_3 and Fe_2O_3 contents of clinopyroxene crystals from Holuhraun and PI-041 that are feasibly in equilibrium with their host glasses are shown in Figure 8A; analyses with $Fe_2O_3 < 0.35$ have been removed as they lie below the effective detection limit of stoichiometric determinations (see Part I). Analyses from Holuhraun show minimal variability, while those from PI-041 are highly variable despite being selected on the basis of being in textural equilibrium with the same glasses; such correlations between Fe_2O_3 and Al_2O_3 would be expected during disequilibrium crystallisation that enhances incorporation of trivalent cations via Tschermak-type substitutions ([Mollo et al, 2010](#); [Ubide et al, 2019](#)).

Current estimates of clinopyroxene-liquid Fe^{3+} partition coefficients (i.e., $D_{Fe^{3+}}^{cpx-liq}$ values) are shown in Figure 8B. [Mallmann and O'Neill \(2009\)](#) and [Davis and Cottrell \(2021\)](#) report constant values of 0.453 ± 0.158 and 0.78 ± 0.30 , respectively. However, Fe was only present at trace levels in the experiments of [Mallmann and O'Neill \(2009\)](#), casting doubt on the suitability of using their $D_{Fe^{3+}}^{cpx-liq}$ value to explain partitioning in OIBs where Fe_2O_3 is a major constituent (>1 wt.%). Similarly, [Davis and Cottrell](#)

(2021) investigated Fe^{3+} partitioning in relatively Fe-poor mantle systems and derived $D_{\text{Fe}^{3+}}^{\text{cpx-liq}}$ indirectly through estimates of Fe–Mg exchange between olivine and clinopyroxene. Rudra and Hirschmann (2022), who directly measured glass and clinopyroxene $\text{Fe}^{3+}/\Sigma\text{Fe}$ contents in the products of experiments on an andesitic starting material at 1–2.5 GPa, therefore provide the best current description of $D_{\text{Fe}^{3+}}^{\text{cpx-liq}}$ that can be applied to OIBs. While the pressures they investigated are somewhat above those relevant for OIB petrogenesis (1–2.5 GPa, versus up to ~ 550 MPa for our samples; Zanon et al, 2020), andesites are compositionally more similar to oceanic basalts than systems designed to investigate mantle melting (cf., Mallmann and O’Neill, 2009; Davis and Cottrell, 2021). Values of $D_{\text{Fe}^{3+}}^{\text{cpx-liq}}$ calculated with the Al_2O_3 - and Fe_2O_3 -dependent Equation 9 of Rudra and Hirschmann (2022) are shown in Figure 9A, and range from ~ 0.2 – 0.3 in Al_2O_3 -poor crystals from Holuhraun up to 1.1 in Al_2O_3 -rich crystals in sample PI-041.

Glass Mg# and $\text{Fe}^{3+}/\Sigma\text{Fe}$ contents estimated from clinopyroxene Fe_2O_3 contents and $D_{\text{Fe}^{3+}}^{\text{cpx-liq}}$ values from Rudra and Hirschmann (2022) are shown in Figure 9. Considerable variability in clinopyroxene Fe_2O_3 contents and $D_{\text{Fe}^{3+}}^{\text{cpx-liq}}$ values across clinopyroxene-glass pairs from Holuhraun and PI-041 translates into comparable variability in estimates of glass Mg# and $\text{Fe}^{3+}/\Sigma\text{Fe}$ contents. Glass $\text{Fe}^{3+}/\Sigma\text{Fe}$ contents of ~ 0.2 estimated for Holuhraun are similar to values reported for other Icelandic tholeiites from Fe-XANES spectroscopy (up to 0.20 for Laki; Hartley et al, 2017). While estimates of glass $\text{Fe}^{3+}/\Sigma\text{Fe}$ contents span a wide range of ~ 0.1 – 0.5 in sample PI-041, most clinopyroxene analyses imply plausible values of ~ 0.3 that are similar to maximum values reported for other OIBs from Fe-XANES spectroscopy (e.g., Moussallam et al, 2019). To provide independent validation of glass $\text{Fe}^{3+}/\Sigma\text{Fe}$ contents estimated from $D_{\text{Fe}^{3+}}^{\text{cpx-liq}}$, we also determined glass $\text{Fe}^{3+}/\Sigma\text{Fe}$ contents from olivine rims by using Equation 10 of Saper et al (2022) to calculate appropriate values of $K_{\text{D,Fe}^{2+}\text{-Mg}}^{\text{ol-liq}}$. Results from olivine-liquid equilibria broadly validate our clinopyroxene-liquid findings for Holuhraun and PI-041, and return estimated glass $\text{Fe}^{3+}/\Sigma\text{Fe}$ contents of ~ 0.20 and ~ 0.32 , respectively.

Glass $\text{Fe}^{3+}/\Sigma\text{Fe}$ contents estimated from $D_{\text{Fe}^{3+}}^{\text{cpx-liq}}$ and $K_{\text{D,Fe}^{2+}\text{-Mg}}^{\text{ol-liq}}$ are shown converted into f_{O_2} in Figure 9B; clinopyroxene-derived values are plotted as kernel density estimates (KDEs) and in the subsequent discussion we discuss the most probable f_{O_2} conditions inferred from KDE peak positions. Conversions between $\text{Fe}^{3+}/\Sigma\text{Fe}$ and f_{O_2} were performed using the model of Borisov et al (2018) and results are reported with respect to the FMQ equilibrium calculated with the model of O’Neill (1987) at temperatures determined from glass MgO contents with Equation 13 from Putirka (2008). Clinopyroxene- and olivine-based approaches return f_{O_2} conditions close to FMQ+1.4 for Holuhraun and centred around FMQ+1.7 to FMQ+2.3 for PI-041; such values are plausible for OIBs evolving under more oxidising conditions than MORBs that have not experienced reductive S degassing (Bali et al, 2018; Hartley et al, 2017; Moussallam et al, 2019). Clinopyroxene oxybarometry that exploits Fe^{3+} partitioning thus appears to be a realistic proposition as long as equilibrium has been maintained – our inability to perform similar calculations on samples from Skuggafjöll serves as a cautionary tale regarding the importance of equilibrium. Although olivine rims and microcrysts from PI-041 record similar f_{O_2} conditions of $\sim \text{FMQ}+2.3$ that align with

conditions estimated from clinopyroxene rims, clinopyroxene microcrysts record lower values of $\sim\text{FMQ}+1.7$. While this divergence may reflect disequilibrium crystallisation, it may also reflect the formation of clinopyroxene microcrysts after the melt had been reduced by S degassing during ascent (Moussallam et al, 2016; Taracsák et al, 2022). Forward models with the MELTS algorithm (Ghiorso and Sack, 1995; Ghiorso et al, 2002) could theoretically be used to further validate relationships between f_{O_2} and clinopyroxene $\text{Fe}^{3+}/\Sigma\text{Fe}$. However, Rudra and Hirschmann (2022) report that MELTS consistently overestimates the Fe^{3+} content of clinopyroxene, likely as a result of clinopyroxene MELTS models being largely calibrated against the products of experiments performed on alkali and highly oxidised compositions (Sack and Ghiorso, 1994). We have therefore decided not to integrate MELTS calculations into our discussion.

Overall, our findings suggest that $D_{\text{Fe}^{3+}}^{\text{cpx-liq}}$ can potentially be used to estimate magmatic f_{O_2} conditions but is currently subject to limitations. The results of our calculations are highly sensitive to the correct identification of equilibrium clinopyroxene-glass pairs. Even when there is strong evidence for textural equilibrium, crystals may not be in chemical equilibrium, resulting in spurious f_{O_2} estimates. The $D_{\text{Fe}^{3+}}^{\text{cpx-liq}}$ model of Rudra and Hirschmann (2022) appears to perform well for analyses from Holuhraun and PI-041 despite their compositional diversity, successfully decoupling clinopyroxene and glass $\text{Fe}^{3+}/\Sigma\text{Fe}$ contents (Figure 9C). Moreover, $D_{\text{Fe}^{3+}}^{\text{cpx-liq}}$ values from Rudra and Hirschmann (2022) lie on a one-to-one line with $D_{\text{Fe}^{3+}}^{\text{cpx-liq}}$ values determined independently via olivine-derived estimates of glass $\text{Fe}^{3+}/\Sigma\text{Fe}$ (Figure 10). Nonetheless, analyses from Holuhraun have a shallower slope on Figure 10 than those from PI-041, suggesting that more work is required to verify that the model of Rudra and Hirschmann (2022) works well for tholeiitic compositions. Nonetheless, the imperfect but encouraging performance of a $D_{\text{Fe}^{3+}}^{\text{cpx-liq}}$ -based oxybarometer highlights the need to experimentally revisit clinopyroxene phase equilibria in diverse basalts under a range of f_{O_2} conditions.

6 Conclusions

By applying the stoichiometric approach for estimating clinopyroxene $\text{Fe}^{3+}/\Sigma\text{Fe}$ described by Droop (1987) and validated in Part I to OIBs from Iceland and the Azores, we demonstrate that Fe^{3+} is one of the most abundant cations in magmatic clinopyroxene crystals after Si, Ca, Mg and Fe^{2+} . Fe_2O_3 is generally present at 1–4 wt.% levels, meaning that Fe^{3+} is a major if cryptic constituent of clinopyroxene crystals from diverse OIBs. On average, clinopyroxene crystals from alkali systems have higher $\text{Fe}^{3+}/\Sigma\text{Fe}$ contents than those from tholeiitic systems, which translate into higher Es contents and, in some cases, non-negligible Ae contents. The incorporation of considerable Ca and Al^{IV} alongside Fe^{3+} has important consequences for the relative proportions of other clinopyroxene components, and DiHd and EnFs in particular, given the cascading effect of forming an additional and previously overlooked component. Trends in clinopyroxene Jd, CaTi and CrAlTs contents can be variably linked to magma compositions (i.e., alkalinity), storage pressures and degrees of evolution. Clinopyroxene Es contents are broadly related to f_{O_2} , with clinopyroxene crystals from alkali systems like Pico evolving under relatively oxidising conditions containing

more Es than those from tholeiitic systems like Holuhraun evolving under relatively reducing conditions.

Using our improved understanding of clinopyroxene $\text{Fe}^{3+}/\Sigma\text{Fe}$ to evaluate Fe–Mg exchange between clinopyroxene crystals and their host glasses demonstrates that our understanding of $K_{\text{D,Fe}^{2+}\text{--Mg}}^{\text{cpx--liq}}$ lags well behind our understanding of $K_{\text{D,Fe}^{2+}\text{--Mg}}^{\text{ol--liq}}$. Although our results suggest that accounting for $\text{Fe}^{3+}/\Sigma\text{Fe}$ in equilibrium clinopyroxene–glass pairs may return viable $K_{\text{D,Fe--Mg}}^{\text{cpx--liq}}$ values under realistic f_{O_2} conditions, they also demonstrate that accounting for Fe^{3+} currently offers no improvement beyond simply assuming that all Fe is present as Fe^{2+} in both phases when considering Fe–Mg exchange. Finally, our exploration of using $D_{\text{Fe}^{3+}}^{\text{cpx--liq}}$ values calculated following Rudra and Hirschmann (2022) for oxybarometry suggests that clinopyroxene crystals have the potential to record magmatic f_{O_2} conditions when clinopyroxene–liquid equilibrium has been preserved during ascent, eruption and quenching. We estimate that magmas erupted from Holuhraun in Iceland and Pico in the Azores evolved at $\sim\text{FMQ}+1.4$ and $\sim\text{FMQ}+2.3$, respectively, consistent with estimates from olivine–liquid equilibria and independent estimates from comparable ocean island systems fed from mantle sources rich in recycled components and appreciably higher than estimates for MORB. Overall, our findings demonstrate that being able to estimate clinopyroxene $\text{Fe}^{3+}/\Sigma\text{Fe}$ routinely will open new opportunities for developing new clinopyroxene–based oxybarometers. They also highlight that new experiments are needed to define $K_{\text{D,Fe}^{2+}\text{--Mg}}^{\text{cpx--liq}}$ and $D_{\text{Fe}^{3+}}^{\text{cpx--liq}}$ systematics over a range of f_{O_2} conditions and magma compositions to ensure that the resulting tools are widely applicable as possible.

Acknowledgements

We thank Lee Paul, David Olivier and Lewis Hughes at the University of Manchester for their help with sample preparation, thin section production and scanning electron microscopy, respectively. We also thank Stuart Kearns and Ben Buse for their help with electron probe microanalysis at the University of Bristol. This work was supported by a NERC Independent Research Fellowship (NE/T011106/1) and Royal Society Research Grant (RGS\R1\201344) to DAN.

References

- Bacon CR, Druitt TH (1988) Compositional evolution of the zoned calcalkaline magma chamber of Mount Mazama, Crater Lake, Oregon. *Contributions to Mineralogy and Petrology* 98:224–256. <https://doi.org/10.1007/BF00402114>
- Bali E, Hartley ME, Halldórsson SA, et al (2018) Melt inclusion constraints on volatile systematics and degassing history of the 2014–2015 Holuhraun eruption, Iceland. *Contributions to Mineralogy and Petrology* 173:9. <https://doi.org/10.1007/s00410-017-1434-1>

- Blundy JD, Melekhova E, Ziberna L, et al (2020) Effect of redox on Fe-Mg-Mn exchange between olivine and melt and an oxybarometer for basalts. *Contributions to Mineralogy and Petrology* 7:103. <https://doi.org/10.1007/s00410-020-01736-7>
- Borisov A, Behrens H, Holtz F (2018) Ferric/ferrous ratio in silicate melts: a new model for 1 atm data with special emphasis on the effects of melt composition. *Contributions to Mineralogy and Petrology* 173(12):98. <https://doi.org/10.1007/s00410-018-1524-8>
- Brounce M, Stolper E, Eiler J (2017) Redox variations in Mauna Kea lavas, the oxygen fugacity of the Hawaiian plume, and the role of volcanic gases in Earth's oxygenation. *Proceedings of the National Academy of Sciences* 114(34):8997–9002. <https://doi.org/10.1073/pnas.1619527114>
- Brounce M, Cottrell E, Kelley KA (2019) The redox budget of the Mariana subduction zone. *Earth and Planetary Science Letters* 528:115859. <https://doi.org/10.1016/j.epsl.2019.115859>
- Brounce M, Stolper E, Eiler J (2022) The mantle source of basalts from Reunion Island is not more oxidized than the MORB source mantle. *Contributions to Mineralogy and Petrology* 177(1):7. <https://doi.org/10.1007/s00410-021-01870-w>
- Burgisser A, Scaillet B (2007) Redox evolution of a degassing magma rising to the surface. *Nature* 445(7124):194–197. <https://doi.org/10.1038/nature05509>
- Canil D, O'Neill HSC (1996) Distribution of Ferric Iron in some Upper-Mantle Assemblages. *Journal of Petrology* 37(3):609–635. <https://doi.org/10.1093/petrology/37.3.609>
- Carmichael ISE (1991) The redox states of basic and silicic magmas: a reflection of their source regions? *Contributions to Mineralogy and Petrology* 106(2):129–141. <https://doi.org/10.1007/BF00306429>
- Cottrell E, Kelley K, Lanzirotti A, et al (2009) High-precision determination of iron oxidation state in silicate glasses using XANES. *Chemical Geology* 268(3-4):167–179. <https://doi.org/10.1016/j.chemgeo.2009.08.008>, publisher: Elsevier B.V. ISBN: 0009-2541
- Cottrell E, Lanzirotti A, Mysen B, et al (2018) A Mössbauer-based XANES calibration for hydrous basalt glasses reveals radiation-induced oxidation of Fe. *American Mineralogist* 103:489–501
- Cottrell E, Birner SK, Brounce M, et al (2022) Oxygen Fugacity Across Tectonic Settings. In: Moretti R, Neuville D (eds) *Magma Redox Geochemistry*, Geophysical Monograph 266. John Wiley & Sons, Inc., p 33–61, <https://doi.org/10.1002/9781119473206.ch3>

- Davis FA, Cottrell E (2021) Partitioning of Fe_2O_3 in peridotite partial melting experiments over a range of oxygen fugacities elucidates ferric iron systematics in mid-ocean ridge basalts and ferric iron content of the upper mantle. *Contributions to Mineralogy and Petrology* 176(9):67. <https://doi.org/10.1007/s00410-021-01823-3>
- Downes MJ (1974) Sector and oscillatory zoning in calcic augites from M. Etna, Sicily. *Contributions to Mineralogy and Petrology* 47(3):187–196. <https://doi.org/10.1007/BF00371538>
- Droop GTR (1987) A general equation for Estimating Fe^{3+} concentrations in ferromagnesian silicates and oxides from microprobe analyses, using stoichiometric criteria. *Mineralogical Magazine* 51(361):431–435. <https://doi.org/10.1180/minmag.1987.051.361.10>
- Evans KA, Tomkins AG (2011) The relationship between subduction zone redox budget and arc magma fertility. *Earth and Planetary Science Letters* 308(3-4):401–409. <https://doi.org/10.1016/j.epsl.2011.06.009>
- Feig ST, Koepke J, Snow JE (2010) Effect of oxygen fugacity and water on phase equilibria of a hydrous tholeiitic basalt. *Contributions to Mineralogy and Petrology* 160(4):551–568. <https://doi.org/10.1007/s00410-010-0493-3>
- França ZT, Tassinari CC, Cruz JV, et al (2006) Petrology, geochemistry and Sr–Nd–Pb isotopes of the volcanic rocks from Pico Island—Azores (Portugal). *Journal of Volcanology and Geothermal Research* 156(1-2):71–89. <https://doi.org/10.1016/j.jvolgeores.2006.03.013>
- Frost BR (1991) Introduction to oxygen fugacity and its petrologic importance. *Reviews in Mineralogy and Geochemistry* 25:1–9
- Gaetani GA (2016) The Behavior of Fe^{3+}/Fe During Partial Melting of Spinel Lherzolite. *Geochimica et Cosmochimica Acta* 185:64–77. <https://doi.org/10.1016/j.gca.2016.03.019>
- Gaillard F, Scaillet B, Arndt NT (2011) Atmospheric oxygenation caused by a change in volcanic degassing pressure. *Nature* 478(7368):229–232. <https://doi.org/10.1038/nature10460>
- Ghiorso MS, Evans BW (2008) Thermodynamics of rhombohedral oxide solid solutions and a revision of the Fe-Ti two-oxide geothermometer and oxygen-barometer. *American Journal of Science* 308(9):957–1039. <https://doi.org/10.2475/09.2008.01>
- Ghiorso MS, Sack RO (1995) Chemical mass transfer in magmatic processes IV. A revised and internally consistent thermodynamic model for the interpolation and extrapolation of liquid-solid equilibria in magmatic systems at elevated temperatures and pressures. *Contributions to Mineralogy and Petrology* 119(2-3):197–212. <https://doi.org/10.1007/BF00307281>

- Ghiorso MS, Hirschmann MM, Reiners PW, et al (2002) The pMELTS: A revision of MELTS for improved calculation of phase relations and major element partitioning related to partial melting of the mantle to 3 GPa. *Geochemistry, Geophysics, Geosystems* 3(5). <https://doi.org/10.1029/2001GC000217>
- Grove TL, Kinzler RJ, Bryan WB (1992) Fractionation of Mid-Ocean Ridge Basalt (MORB). In: *Mantle Flow and Melt Generation at Mid-Ocean Ridges*, Geophysical Monograph 71. American Geophysical Union, Washington D.C., p 281–310, <https://doi.org/10.1029/GM071>
- Halldórsson SA, Bali E, Hartley ME, et al (2018) Petrology and geochemistry of the 2014–2015 Holuhraun eruption, central Iceland: compositional and mineralogical characteristics, temporal variability and magma storage. *Contributions to Mineralogy and Petrology* 173:64. <https://doi.org/10.1007/s00410-018-1487-9>
- Hartley ME, Shorttle O, MacLennan J, et al (2017) Olivine-hosted melt inclusions as an archive of redox heterogeneity in magmatic systems. *Earth and Planetary Science Letters* 479:192–205. <https://doi.org/10.1016/j.epsl.2017.09.029>
- Holland HD (2002) Volcanic gases, black smokers, and the great oxidation event. *Geochimica et Cosmochimica Acta* 66(21):3811–3826. [https://doi.org/10.1016/S0016-7037\(02\)00950-X](https://doi.org/10.1016/S0016-7037(02)00950-X)
- Hughes EC, Saper L, Liggins P, et al (2023) The sulfur solubility minimum and maximum in silicate melt. *Journal of the Geological Society* pp 1–50. <https://doi.org/10.1144/jgs2021-125>
- Jochum KP, Willbold M, Raczek I, et al (2005) Chemical characterisation of the USGS reference glasses GSA-1G, GSC-1G, GSD-1G, GSE-1G, BCR-2G, BHVO-2G and BIR-1G using EPMA, ID-TIMS, ID-ICP-MS and LA-ICP-MS. *Geostandards and Geoanalytical Research* 29:285–302
- Jugo PJ (2009) Sulfur content at sulfide saturation in oxidized magmas. *Geology* 37(5):415–418. <https://doi.org/10.1130/G25527A.1>
- Kelley KA, Cottrell E (2009) Water and the Oxidation State of Subduction Zone Magmas. *Science* 325(5940):605–607. <https://doi.org/10.1126/science.1174156>
- Kress VC, Carmichael ISE (1991) The compressibility of silicate liquids containing Fe₂O₃ and the effect of composition, temperature, oxygen fugacity and pressure on their redox states. *Contributions to Mineralogy and Petrology* 108(1-2):82–92. <https://doi.org/10.1007/BF00307328>
- Larsen LM (1976) Clinopyroxenes and Coexisting Mafic Minerals from the Alkaline Ilimaussaq Intrusion, South Greenland. *Journal of Petrology* 17(2):258–290. <https://doi.org/10.1093/petrology/17.2.258>

- Leung IS (1974) Sector-zoned Titanaugites: Morphology, Crystal Chemistry, and Growth. *American Mineralogist* 59:127–138
- Lindsley DH (1983) Pyroxene thermometry. *American Mineralogist* 68(5-6):477–493. <https://doi.org/10.1007/BF00372872>
- Lindsley DH, Andersen DJ (1983) A two-pyroxene thermometer. *Journal of Geophysical Research* 88 Suppl:A887–A906. <https://doi.org/10.1029/JB088iS02p0A887>
- Loughlin SC (1995) The evolution of the Eyjafjöll volcanic system, southern Iceland. PhD, Durham University, Durham
- Luth RW, Canil D (1993) Ferric iron in mantle-derived pyroxenes and a new oxybarometer for the mantle. *Contributions to Mineralogy and Petrology* 113(2):236–248. <https://doi.org/10.1007/BF00283231>
- Mallmann G, O'Neill HSC (2009) The crystal/melt partitioning of V during mantle melting as a function of oxygen fugacity compared with some other elements (Al, P, Ca, Sc, Ti, Cr, Fe, Ga, Y, Zr and Nb). *Journal of Petrology* 50(9):1765–1794. <https://doi.org/10.1093/petrology/egp053>
- McCammon C (2021) Mössbauer Spectroscopy with High Spatial Resolution: Spotlight on Geoscience. In: Yoshida Y, Langouche G (eds) *Modern Mössbauer Spectroscopy*, vol 137. Springer Singapore, Singapore, p 221–266, https://doi.org/10.1007/978-981-15-9422-9_5
- McCanta MC, Dyar MD, Rutherford MJ, et al (2004) Iron partitioning between basaltic melts and clinopyroxene as a function of oxygen fugacity. *American Mineralogist* 89(11-12):1685–1693. <https://doi.org/10.2138/am-2004-11-1214>, ISBN: 0003-004X
- McGuire AV, Dyar MD, Ward KA (1989) Neglected $\text{Fe}^{3+}/\text{Fe}^{2+}$ ratios – a study of Fe^{3+} content of megacrysts from alkali basalts. *Geology* 17(8):687–690. [https://doi.org/10.1130/0091-7613\(1989\)017<0687:NFFRAS>2.3.CO](https://doi.org/10.1130/0091-7613(1989)017<0687:NFFRAS>2.3.CO)
- Mollo S, Del Gaudio P, Ventura G, et al (2010) Dependence of clinopyroxene composition on cooling rate in basaltic magmas: Implications for thermobarometry. *Lithos* 118(3-4):302–312. <https://doi.org/10.1016/j.lithos.2010.05.006>
- Mollo S, Blundy JD, Scarlato P, et al (2018) An integrated P-T- H_2O -lattice strain model to quantify the role of clinopyroxene fractionation on REE+Y/HFSE patterns of mafic alkaline magmas: Application to eruptions at Mt. Etna. *Earth-Science Reviews* 185:32–56. <https://doi.org/10.1016/j.earscirev.2018.05.014>
- Morimoto N, Fabries J, Ferguson AK, et al (1988) Nomenclature of pyroxenes. *American Mineralogist* 73:1123–1133. <https://doi.org/10.1007/BF01226262>

- Moussallam Y, Oppenheimer C, Scaillet B, et al (2014) Tracking the changing oxidation state of Erebus magmas, from mantle to surface, driven by magma ascent and degassing. *Earth and Planetary Science Letters* 393:200–209. <https://doi.org/10.1016/j.epsl.2014.02.055>
- Moussallam Y, Edmonds M, Scaillet B, et al (2016) The impact of degassing on the oxidation state of basaltic magmas: A case study of Kilauea volcano. *Earth and Planetary Science Letters* 450:317–325. <https://doi.org/10.1016/j.epsl.2016.06.031>
- Moussallam Y, Longpré MA, McCammon CA, et al (2019) Mantle plumes are oxidised. *Earth and Planetary Science Letters* 527:115798. <https://doi.org/10.1016/j.epsl.2019.115798>
- Nash WM, Smythe DJ, Wood BJ (2019) Compositional and temperature effects on sulfur speciation and solubility in silicate melts. *Earth and Planetary Science Letters* 507:187–198. <https://doi.org/10.1016/j.epsl.2018.12.006>
- Neave DA, MacLennan J (2020) Clinopyroxene Dissolution Records Rapid Magma Ascent. *Frontiers in Earth Science* 8:188. <https://doi.org/10.3389/feart.2020.00188>
- Neave DA, Putirka KD (2017) A new clinopyroxene-liquid barometer, and implications for magma storage pressures under Icelandic rift zones. *American Mineralogist* 102:777–794. <https://doi.org/10.2138/am-2017-5968>
- Neave DA, Passmore E, MacLennan J, et al (2013) Crystal-melt relationships and the record of deep mixing and crystallization in the AD 1783 Laki eruption, Iceland. *Journal of Petrology* 54(8):1661–1690. <https://doi.org/10.1093/petrology/egt027>
- Neave DA, MacLennan J, Hartley ME, et al (2014) Crystal storage and transfer in basaltic systems: the Skuggafjöll eruption, Iceland. *Journal of Petrology* 55(12):2311–2346. <https://doi.org/10.1093/petrology/egu058>
- Neave DA, Bali E, Guðfinnsson GH, et al (2019a) Clinopyroxene–liquid equilibria and geothermobarometry in natural and experimental tholeiites: the 2014–2015 Holuhraun eruption, Iceland. *Journal of Petrology* 60:1653–1680. <https://doi.org/10.1093/petrology/egz042>
- Neave DA, Namur O, Shorttle O, et al (2019b) Magmatic evolution biases basaltic records of mantle chemistry towards melts from recycled sources. *Earth and Planetary Science Letters* 520:199–211. <https://doi.org/10.1016/j.epsl.2019.06.003>
- Nikkola P, Bali E, Kahl M, et al (2019) Mid-crustal storage and crystallization of Eyjafjallajökull. *Jökull* 69:77–96
- O’Neill HSC (1987) Quartz-fayalite-iron and quartz-fayalite-magnetite equilibria and the free energy of formation of fayalite (Fe_2SiO_4) and magnetite (Fe_3O_4). *American Mineralogist* 72(1-2):67–75

- O'Neill HSC (2021) The Thermodynamic Controls on Sulfide Saturation in Silicate Melts with Application to Ocean Floor Basalts. In: Neuvill DR, Moretti R (eds) *Magma Redox Geochemistry*, Geophysical Monograph 266. American Geophysical Union, Washington D.C., p 177–213, <https://doi.org/10.1002/9781119473206.ch10>
- O'Neill HSC, Berry AJ, Mallmann G (2018) The oxidation state of iron in Mid-Ocean Ridge Basaltic (MORB) glasses: Implications for their petrogenesis and oxygen fugacities. *Earth and Planetary Science Letters* 504:152–162. <https://doi.org/10.1016/j.epsl.2018.10.002>
- Oppenheimer C, Moretti R, Kyle PR, et al (2011) Mantle to surface degassing of alkalic magmas at Erebus volcano, Antarctica. *Earth and Planetary Science Letters* 306(3-4):261–271. <https://doi.org/10.1016/j.epsl.2011.04.005>
- Passmore E, MacLennan J, Fitton JG, et al (2012) Mush disaggregation in basaltic magma chambers: Evidence from the AD 1783 Laki eruption. *Journal of Petrology* 53(12):2593–2623. <https://doi.org/10.1093/petrology/egs061>
- Putirka KD (2008) Thermometers and Barometers for Volcanic Systems. *Reviews in Mineralogy and Geochemistry* 69(1):61–120. <https://doi.org/10.2138/rmg.2008.69.3>
- Putirka KD, Johnson M, Kinzler RJ, et al (1996) Thermobarometry of mafic igneous rocks based on clinopyroxene-liquid equilibria, 0–30 kbar. *Contributions to Mineralogy and Petrology* 123(1):92–108. <https://doi.org/10.1007/s004100050145>
- Reay A, Johnstone R, Kawachi Y (1989) Kaersutite, a possible international microprobe standard. *Geostandards and Geoanalytical Research* 13(1):187–190. <https://doi.org/10.1111/j.1751-908X.1989.tb00471.x>
- Robinson P (1980) The composition space of terrestrial pyroxenes -internal and external limits. *Reviews in Mineralogy and Geochemistry* 7:419–494. <https://doi.org/10.1515/9781501508257-013>
- Roeder PL, Emslie RF (1970) Olivine-liquid equilibrium. *Contributions to Mineralogy and Petrology* 29(4):275–289. <https://doi.org/10.1007/BF00371276>
- Rudra A, Hirschmann MM (2022) Fe³⁺ partitioning between clinopyroxene and silicate melt at 1-2.5 GPa: implications for Fe³⁺ content of MORB and OIB source mantle. *Geochimica et Cosmochimica Acta* 328:258–279. <https://doi.org/10.1016/j.gca.2022.04.023>
- Rudra A, Cottrell E, Hirschmann MM (2021) Experimental determination of ferric iron partitioning between pyroxene and melt at 100 kPa. *Chemical Geology* 584:120532. <https://doi.org/10.1016/j.chemgeo.2021.120532>
- Sack RO, Ghiorso MS (1994) Thermodynamics of multicomponent pyroxenes: III. Calibration of Fe²⁺(Mg)₋₁, TiAl₂(MgSi₂)₋₁, TiFe³⁺₂(MgSi₂)₋₁, AlFe³⁺(MgSi)₋₁,

- NaAl(CaMg)₋₁, Al₂(MgSi)₋₁ and Ca(Mg)₋₁ exchange reactions between pyroxenes and silicate melts. *Contributions to Mineralogy and Petrology* 118(3):271–296. <https://doi.org/10.1007/BF00306648>
- Saper LM, Stolper MB, Baker EM (2022) Fe²⁺–Mg partitioning between olivine and liquid at low oxygen fugacity: an experimental and thermodynamic framework. *Contributions to Mineralogy and Petrology* 177:94. <https://doi.org/10.1007/s00410-022-01955-0>
- Shorttle O, Moussallam Y, Hartley ME, et al (2015) Fe-XANES analyses of Reykjanes Ridge basalts: Implications for oceanic crust’s role in the solid Earth oxygen cycle. *Earth and Planetary Science Letters* 427:272–285. <https://doi.org/10.1016/j.epsl.2015.07.017>
- Stracke A (2012) Earth’s heterogeneous mantle: A product of convection-driven interaction between crust and mantle. *Chemical Geology* 330–331:274–299. <https://doi.org/10.1016/j.chemgeo.2012.08.007>
- Taracsák Z, Longpré MA, Tartèse R, et al (2022) Highly oxidising conditions in volatile-rich El Hierro magmas: implications for ocean island magmatism. *Journal of Petrology* <https://doi.org/10.1093/petrology/egac011>
- Thomson A, MacLennan J (2013) The distribution of olivine compositions in Icelandic basalts and picrites. *Journal of Petrology* 54(4):745–768. <https://doi.org/10.1093/petrology/egs083>
- Toplis MJ, Carroll MR (1995) An Experimental Study of the Influence of Oxygen Fugacity on Fe-Ti Oxide Stability, Phase Relations, and Mineral-Melt Equilibria in Ferro-Basaltic Systems. *Journal of Petrology* 36(5):1137–1170. URL <http://petrology.oxfordjournals.org/content/36/5/1137.abstract>
- Ubide T, Mollo S, Zhao JX, et al (2019) Sector-zoned clinopyroxene as a recorder of magma history, eruption triggers, and ascent rates. *Geochimica et Cosmochimica Acta* 251:265–283. <https://doi.org/10.1016/j.gca.2019.02.021>
- Wang X, Hou T, Wang M, et al (2021) A new clinopyroxene thermobarometer for mafic to intermediate magmatic systems. *European Journal of Mineralogy* 33(5):621–637. <https://doi.org/10.5194/ejm-33-621-2021>
- Weis FA, Skogby H, Troll VR, et al (2015) Magmatic water contents determined through clinopyroxene: Examples from the Western Canary Islands, Spain. *Geochemistry, Geophysics, Geosystems* 16:2127–2146. <https://doi.org/10.1002/2015GC005800>
- Wieser P, Kent A, Till C (2022) Barometers behaving badly II: A critical evaluation of Cpx-only and Cpx-Liq thermobarometry in variably-hydrous arc magmas. *EarthArXiv* <https://doi.org/10.31223/X59655>

- Wieser PE, Kent AJR, Till CB, et al (2023) Barometers Behaving Badly I: Assessing the Influence of Analytical and Experimental Uncertainty on Clinopyroxene Thermobarometry Calculations at Crustal Conditions. *Journal of Petrology* 64(2):1–27. <https://doi.org/10.1093/petrology/egac126>
- Wood BJ, Blundy JD (1997) A predictive model for rare earth element partitioning between clinopyroxene and anhydrous silicate melt. *Contributions to Mineralogy and Petrology* 129(2-3):166–181. <https://doi.org/10.1007/s004100050330>
- Wood BJ, Walter MJ, Wade J (2006) Accretion of the Earth and segregation of its core. *Nature* 441(7095):825–833. <https://doi.org/10.1038/nature04763>
- Zanon V, Pimentel A, Auxerre M, et al (2020) Unravelling the magma feeding system of a young basaltic oceanic volcano. *Lithos* 352-353:105325. <https://doi.org/10.1016/j.lithos.2019.105325>
- Zhang HL, Cottrell E, Solheid PA, et al (2018) Determination of Fe³⁺/Fe of XANES basaltic glass standards by Mössbauer spectroscopy and its application to the oxidation state of iron in MORB. *Chemical Geology* 479:166–175. <https://doi.org/10.1016/j.chemgeo.2018.01.006>
- Zindler A, Hart SR (1986) Chemical Geodynamics. *Annual Reviews of Earth and Planetary Sciences* 14(1):493–571. <https://doi.org/10.1146/annurev.earth.14.1.493>

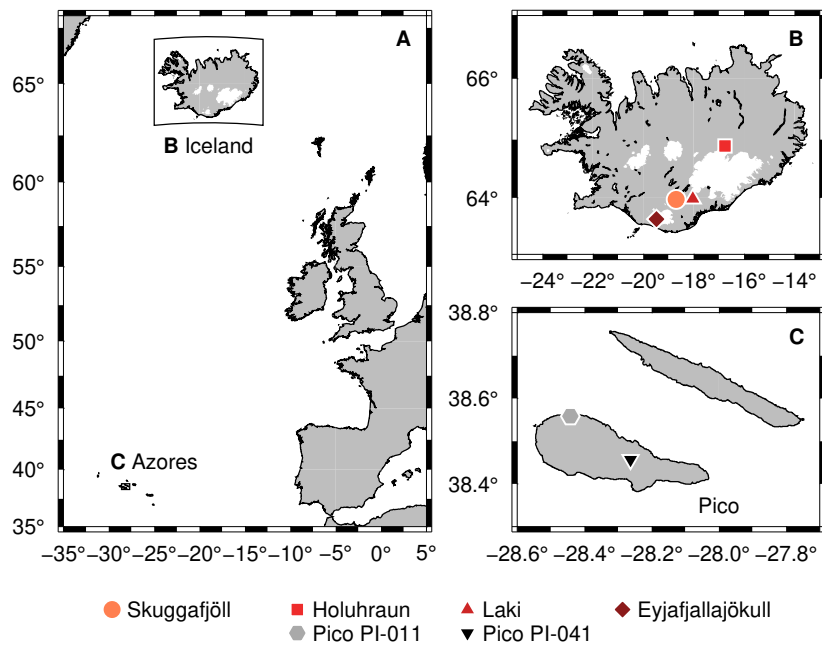


Fig. 1: (A) Map of the North Atlantic region encompassing sample locations in Iceland and the Azores. (B) Map of Iceland showing the location of samples from Skuggafjöll, Holuhraun, Laki and Eyjafjallajökull. (C) Map of part of the Azores archipelago showing the location of samples on Pico Island.

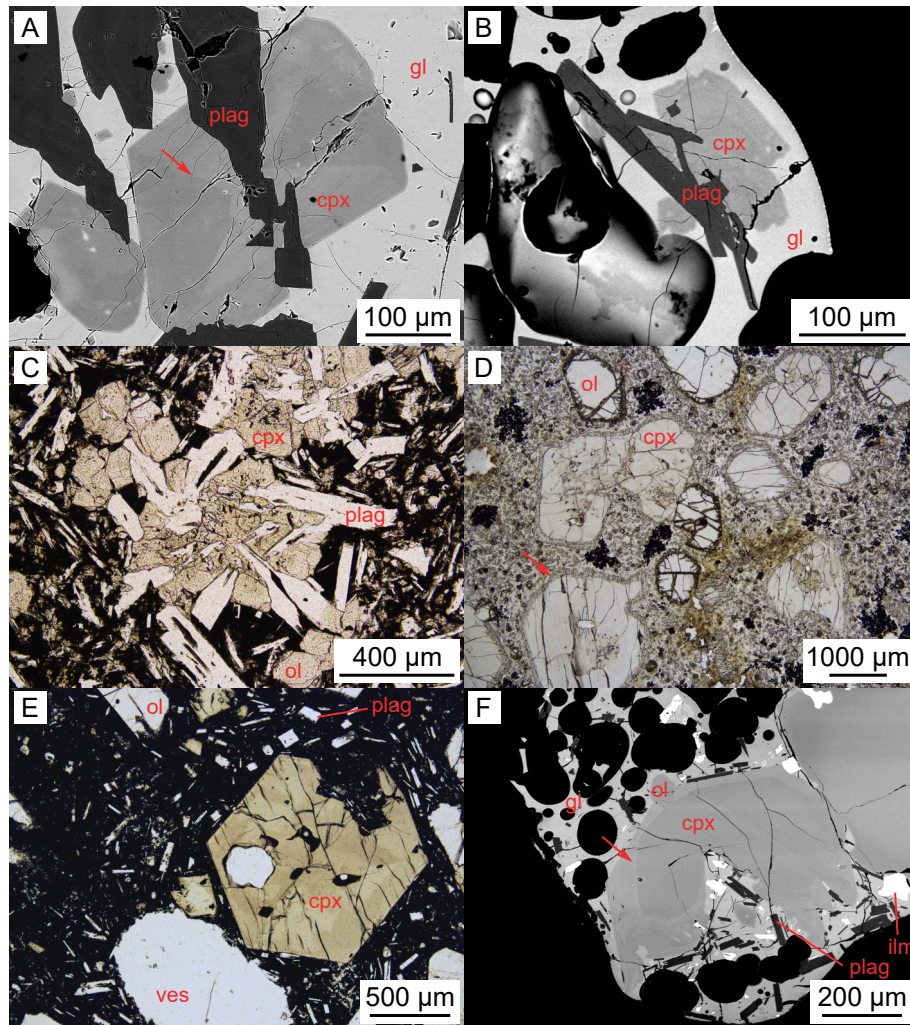


Fig. 2: Clinopyroxene textures in ocean island basalts. Labels are as follows: cpx, clinopyroxene; ol, olivine; plag, plagioclase; gl, glass; ilm, ilmenite; and ves, vesicle. (A) Backscattered electron (BSE) image of clinopyroxene in pillow basalt HOR-11-01 from Skuggafjöll. An interface between low-BSE-intensity $\{111\}$ sectors and high-BSE-intensity $\{hk0\}$ is highlighted with an arrow. (B) BSE image of ophitic clinopyroxene in a basaltic tephra sample from Holuhraun. (C) Photomicrograph of clinopyroxene in ophitic arrangement in basaltic lava sample LAK-04 from Laki. (D) Photomicrograph of large clinopyroxene macrocrysts in ankaramitic lava sample HVAM13-01 from Eyjafjallajökull. The arrow shows rims undergoing dissolution (e.g., [Neave and MacLennan, 2020](#)). (E) Photomicrograph of large clinopyroxene macrocrysts in basaltic lava sample PI-011 from Pico, Azores. Sector zoning is prominent and highlighted with the arrow. (F) BSE image of large clinopyroxene macrocrysts in basaltic tephra sample PI-041 from Pico, Azores. A prominent concentric zoning boundary is highlighted with the arrow.

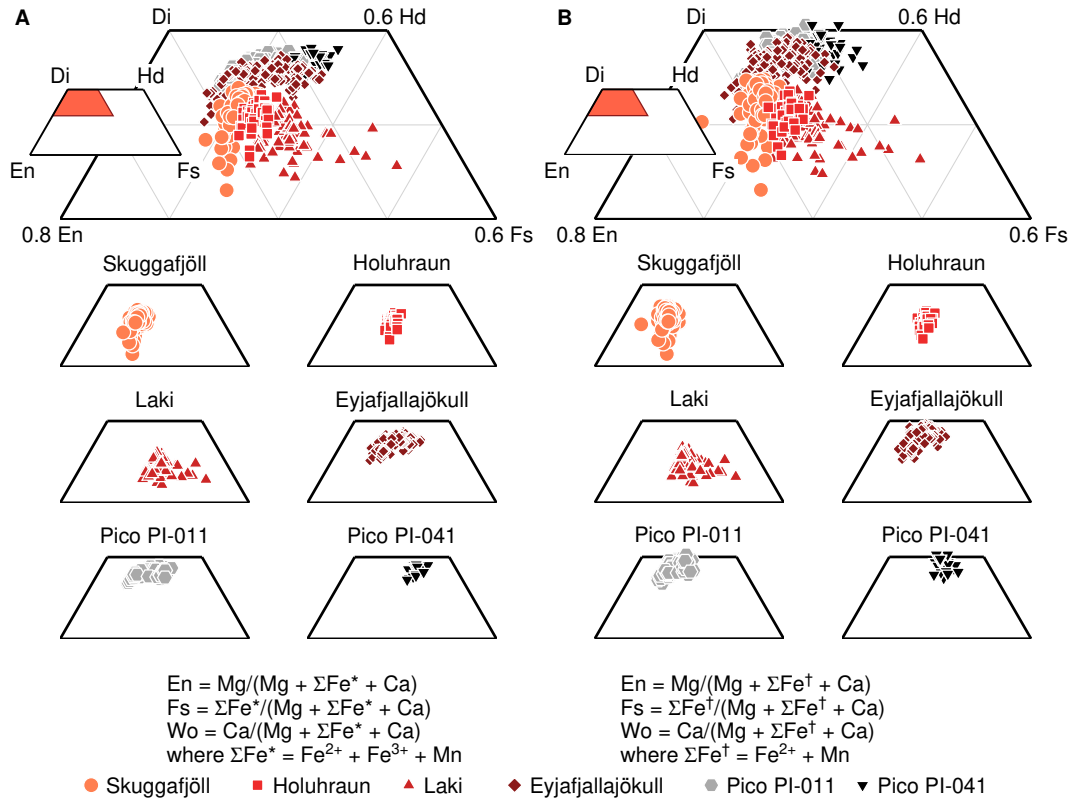


Fig. 3: Summary of clinopyroxene compositions from Iceland and the Azores. (A) Pyroxene quadrilateral showing clinopyroxene quadrilateral components (diopside, Di; hedenbergite, Hd; enstatite, En; and ferrosilite, Fs) calculated following Morimoto et al (1988) where the Fe component (ΣFe^*) is equal to the sum of Fe^{2+} , Fe^{3+} and Mn. (B) Pyroxene quadrilateral showing adjusted clinopyroxene quadrilateral components (diopside, Di^\dagger ; hedenbergite, Hd^\dagger ; enstatite, En^\dagger ; and ferrosilite, Fs^\dagger) calculated following Morimoto et al (1988) where the Fe component (ΣFe^\dagger) is equal to the sum of Fe^{2+} and Mn, with Fe^{2+} determined by stoichiometry following Droop (1987).

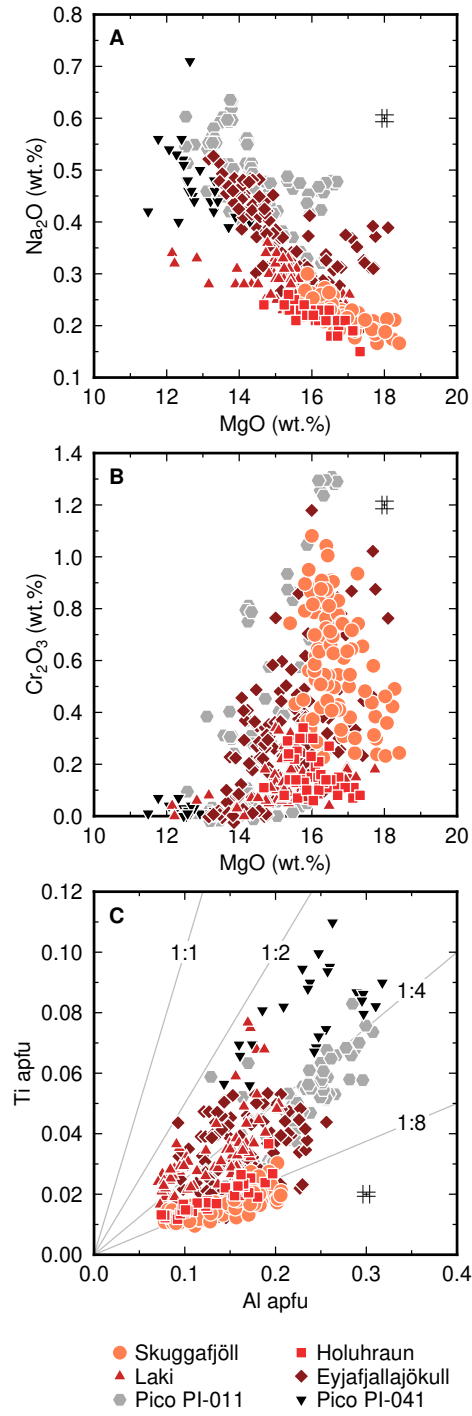


Fig. 4: Summary of key non-quadrilateral major elements in clinopyroxene crystals from ocean island basalts; 1σ analytical uncertainties are shown. (A) Variation in Na_2O as a function of MgO . (B) Variation in Cr_2O_3 as a function of MgO . (C) Covariation of Ti and Al calculated on a basis of six oxygens.

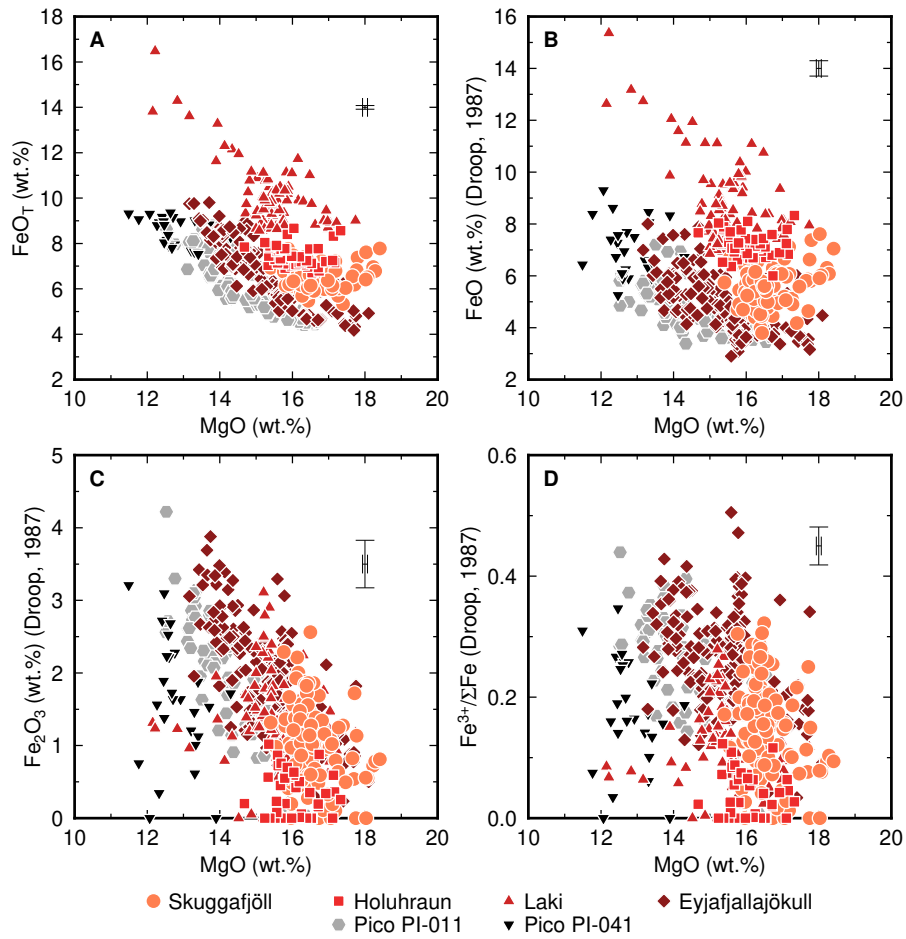


Fig. 5: Iron concentration and valence systematics in clinopyroxene crystals from Iceland and the Azores; 1σ analytical uncertainties are shown. (A) MgO versus total Fe expressed as FeO (FeO_T). (B) MgO versus FeO determined by stoichiometry following Droop (1987). (C) MgO versus Fe_2O_3 determined by stoichiometry following Droop (1987). (D) MgO versus $\text{Fe}^{3+}/\Sigma\text{Fe}$ determined by stoichiometry following Droop (1987).

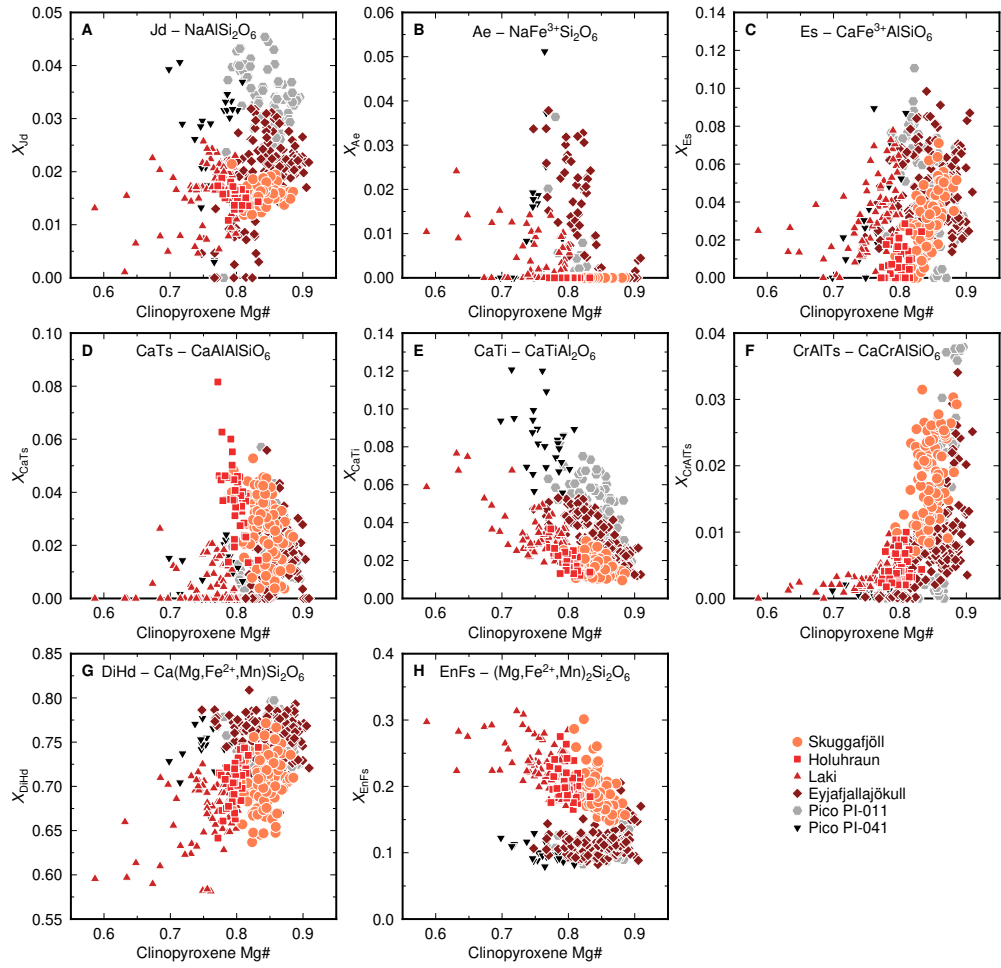


Fig. 6: Clinopyroxene components in clinopyroxene crystals from Iceland and the Azores. Clinopyroxene Mg# is expressed as $\text{Mg}/(\text{Mg}+\text{Fe}^{2+})$ with Fe^{2+} determined following Droop (1987). The scheme for calculating the following components is described in the main text: (A) jadeite, Jd; (B) aegirine, Ae; neptunite, Np; (C) esseneite, Es; (D) calcium-Tschermak's component, CaTs; (E) titanian calcium-Tschermak's component, CaTi; (F) chromian calcium-Tschermak's component, CrCaTs; (G) diopside and hedenbergite, DiHd; and (H) enstatite and ferrosilite, EnFs.

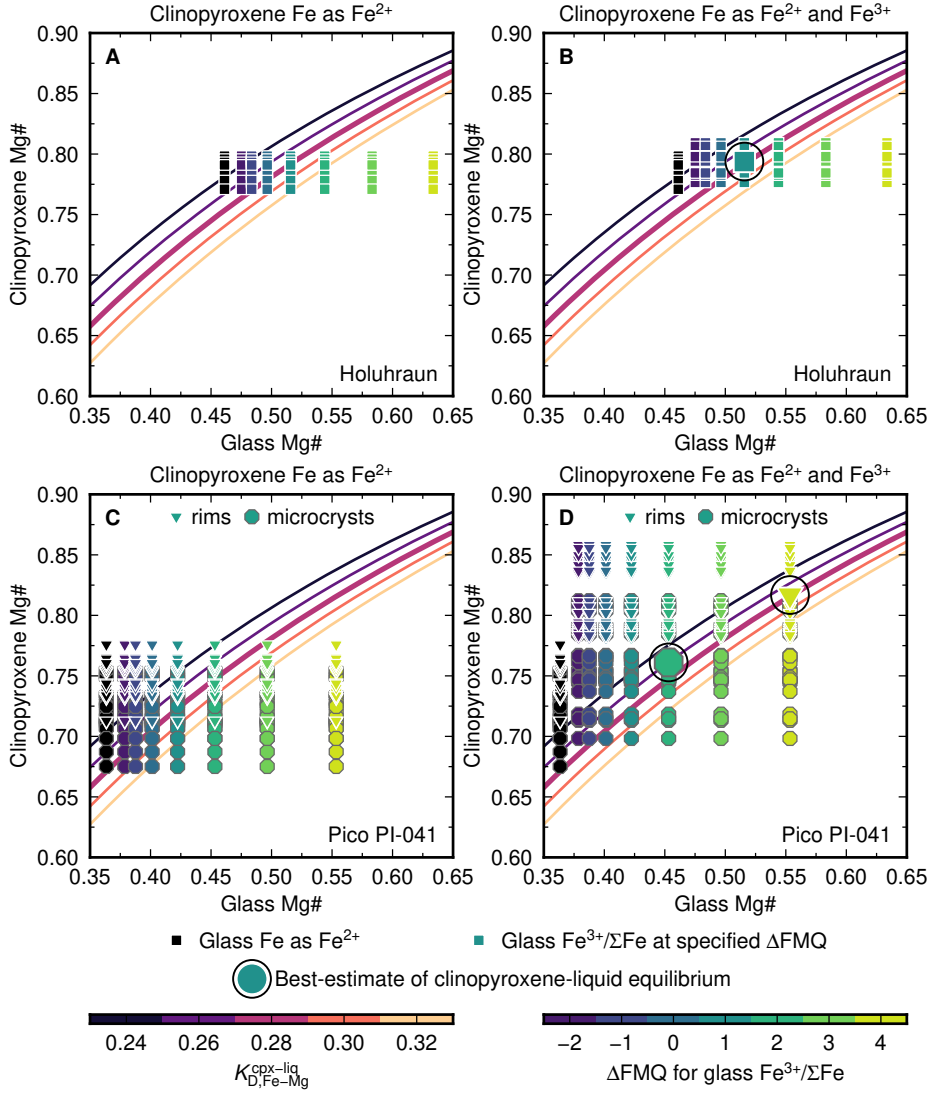


Fig. 7: Summary of Fe–Mg exchange between clinopyroxene crystals and their host glasses: (A and B) Holuhraun and (C and D) Pico PI-041). Coloured lines show $K_{D,Fe-Mg}^{cpx-liq}$ values, with a value of 0.28 determined with Eq. 35 of Putirka (2008) at 1200°C shown highlighted with a thicker line. Best estimates of oxygen fugacity (f_{O_2}) conditions from clinopyroxene-liquid equilibria are shown with large symbols; these reflect where mean clinopyroxene compositions most closely approach $K_{D,Fe-Mg}^{cpx-liq} = 0.28$ at a given f_{O_2} . (A and C) Fe²⁺–Mg exchange between clinopyroxene crystals and their host glasses with glass Fe³⁺/ Σ Fe at a range of f_{O_2} conditions (expressed relative to the fayalite-magnetite-quartz equilibrium; ΔFMQ) according to Borisov et al (2018) and all Fe in clinopyroxene crystals expressed as Fe²⁺. (B and D) Fe²⁺–Mg exchange between clinopyroxene crystals and their host glasses with glass Fe³⁺/ Σ Fe contents at a range of oxygen fugacities and Fe in clinopyroxene crystals expressed as Fe²⁺ determined by stoichiometry following Droop (1987).

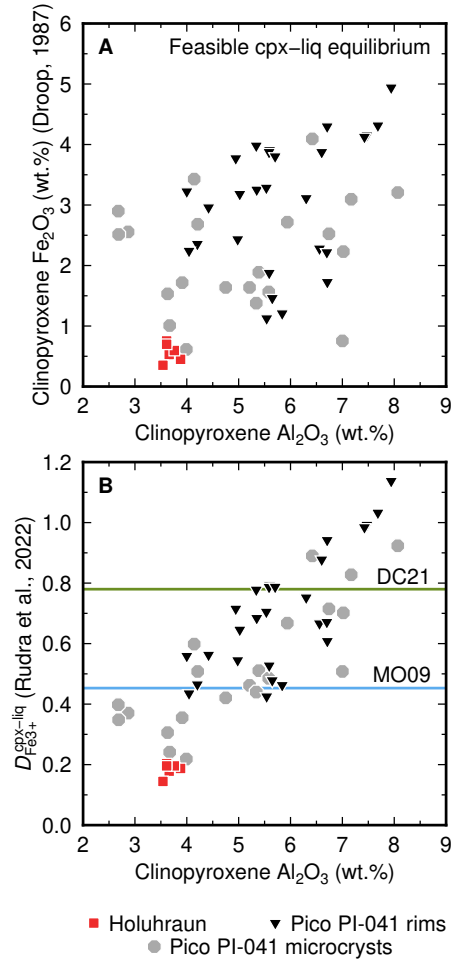


Fig. 8: (A) Combined Al₂O₃ and Fe₂O₃ systematics in clinopyroxene crystals feasibly in equilibrium with their host glasses. Rim and microcryst analyses in PI-041 from Pico were selected on the basis of their textural associations; analyses from Holuhraun were selected from $\{hk0\}$ prism sectors thought to record clinopyroxene–liquid equilibrium (Neave and Putirka, 2017; Neave et al, 2019b). (B) Ferric iron partition coefficients ($D_{\text{Fe}^{3+}}^{\text{cpx-liq}}$) estimated with the model of Rudra and Hirschmann (2022) that depends on clinopyroxene Al₂O₃ and Fe₂O₃ contents, compared with constant values from Mallmann and O’Neill (2009) (MO09) and Davis and Cottrell (2021) (DC21).

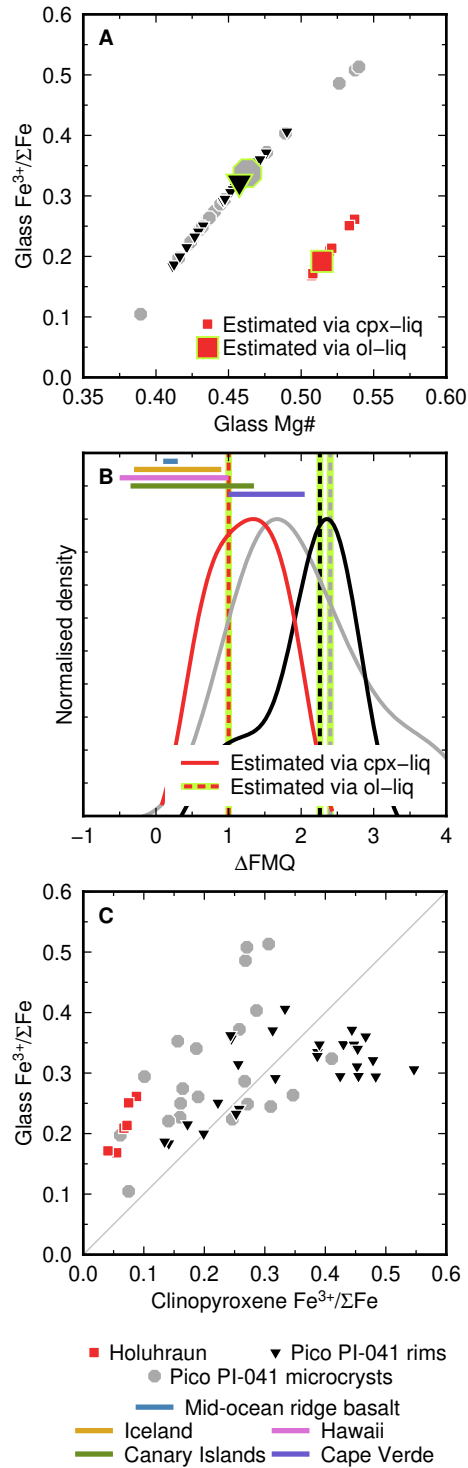


Fig. 9: The potential for clinopyroxene-based oxybarometry. (A) Glass Mg# values and $\text{Fe}^{3+}/\Sigma\text{Fe}$ contents estimated using observed clinopyroxene Fe^{3+} determined with the approach of Droop (1987) and $D_{\text{Fe}^{3+}}^{\text{cpx-liq}}$ values estimated with the model of Rudra and Hirschmann (2022). Large symbols show values determined from olivine-liquid equilibria with the $K_{\text{D,Fe-Mg}}^{\text{ol-liq}}$ model of Saper et al (2022). (B) Kernel density estimates of glass $\text{Fe}^{3+}/\Sigma\text{Fe}$ contents from A converted into oxygen fugacities relative to the fayalite-magnetite-quartz equilibrium (ΔFMQ) using the model of Borisov et al (2018); FMQ calculated following O'Neill (1987) with temperatures determined from glass MgO contents with Equation. 13 from Putirka (2008). Vertical dashed lines show oxygen fugacities estimated from olivine-liquid equilibria. Horizontal lines show oxygen fugacity estimates from the following sources: mid-ocean ridge basalt, Zhang et al (2018); Iceland, Hartley et al (2017); Hawaii, Moussallam et al (2016) and Brounce et al (2017); and Canary Islands and Cape Verde Moussallam et al (2019). (C) Relationship between clinopyroxene $\text{Fe}^{3+}/\Sigma\text{Fe}$ contents and estimated glass $\text{Fe}^{3+}/\Sigma\text{Fe}$ contents.

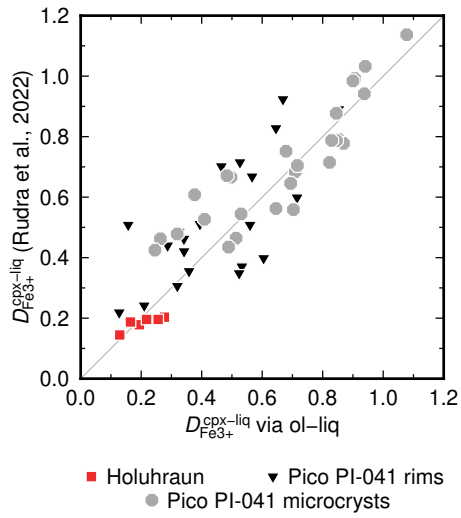


Fig. 10: Comparison between $D_{\text{Fe}^{3+}}^{\text{cpx-liq}}$ values estimated with the model of Rudra and Hirschmann (2022) and those estimated from glass $\text{Fe}^{3+}/\Sigma\text{Fe}$ contents estimated via olivine-liquid equilibria described using the $K_{\text{D,Fe-Mg}}^{\text{ol-liq}}$ model of Saper et al (2022).

Appendix A Scheme for assigning clinopyroxene components

The following scheme for assigning clinopyroxene components is described in Part I and repeated here for reference:

1. Calculate clinopyroxene cation fractions (X_{cation}) from oxide concentrations on a six oxygen basis
2. Determine clinopyroxene $X_{\text{Fe}^{2+}}$ and $X_{\text{Fe}^{3+}}$ contents following Droop (1987) encompassing the renormalisation of cations (including total Fe) by multiplying each cation by T/S as outlined in his point (iv); the total number of all original cations will now equal four and values of $X_{\text{Fe}^{2+}}$ and $X_{\text{Fe}^{3+}}$ can be used to convert FeO_T into FeO and Fe_2O_3
3. Determine the relative proportions of tetrahedral and octahedral Al (Al^{IV} and Al^{VI} , respectively) such that $X_{\text{Al}^{\text{IV}}} = 2 - X_{\text{Si}}$ and $X_{\text{Al}^{\text{VI}}} = X_{\text{Al}} - X_{\text{Al}^{\text{IV}}}$; if X_{Si} exceeds 2 there is no $X_{\text{Al}^{\text{IV}}}$
4. Form Jd ($\text{NaAlSi}_2\text{O}_6$) from whichever is less between Na and Al^{VI} such that $X_{\text{Jd}} = X_{\text{Na}}$ or $X_{\text{Jd}} = X_{\text{Al}^{\text{VI}}}$
5. Form Ae ($\text{NaFe}^{3+}\text{Si}_2\text{O}_6$) from whichever is less between Na remaining after Jd formation and Fe^{3+} such that $X_{\text{Ae}} = X_{\text{Na}} - X_{\text{Jd}}$ or $X_{\text{Ae}} = X_{\text{Fe}^{3+}}$
6. Form Np ($\text{NaFe}_{0.5}^{2+}\text{Ti}_{0.5}\text{Si}_2\text{O}_6$) from any Na remaining after Ae formation such that $X_{\text{Np}} = X_{\text{Na}} - X_{\text{Jd}} - X_{\text{Ae}}$; only relevant for alkali clinopyroxenes
7. Form Es ($\text{CaFe}^{3+}\text{AlSiO}_6$) from any Fe^{3+} remaining after Ae formation such that $X_{\text{Es}} = X_{\text{Fe}^{3+}} - X_{\text{Ae}}$
8. Form CaTs (CaAlAlSiO_6) from any $X_{\text{Al}^{\text{VI}}}$ remaining after Jd formation such that $X_{\text{CaTs}} = X_{\text{Al}^{\text{VI}}} - X_{\text{Jd}}$
9. Form CaTi ($\text{CaTiAl}_2\text{O}_6$) from any Ti remaining after Np formation such that $X_{\text{CaTi}} = X_{\text{Ti}} - X_{\text{Np}}/2$; Np is only present in alkali clinopyroxenes
10. Form CrAlTs (CaCrAlSiO_6) from Cr such that $X_{\text{CrAlTs}} = X_{\text{Cr}}$
11. Form DiHd ($\text{Ca}(\text{Mg}, \text{Fe}^{2+}, \text{Mn})\text{Si}_2\text{O}_6$) from any Ca remaining after Es, CaTs, CaTi and CrAlTs formation such that $X_{\text{DiHd}} = X_{\text{Ca}} - X_{\text{Es}} - X_{\text{CaTs}} - X_{\text{CaTi}} - X_{\text{CrAlTs}}$
12. Form EnFs ($(\text{Mg}, \text{Fe}^{2+}, \text{Mn})_2\text{Si}_2\text{O}_6$) from any Mg, Fe^{2+} and Mn remaining after DiHd formation such that $X_{\text{EnFs}} = (X_{\text{Mg}} + X_{\text{Fe}^{2+}} + X_{\text{Mn}}) - X_{\text{DiHd}}/2$